SPECIAL
Air-sea interaction during PISTON-MISOBOB-CAMP2Ex
COLLECTION

Intraseasonal Variability of Upper-Ocean Heat Fluxes in the Central Bay of Bengal

HEMANTHA W. WIJESEKERA,[a] W. J. TEAGUE,[b] DAVID W. WANG,[a] Z. R. HALLOCK,[b] CONRAD A. LUECKE,[c] EWA JAROSZ,[a] H. J. S. FERNANDO,[d] S. U. P. JINADASA,[e] TOMMY G. JENSEN,[a] ADAM RYDBECK,[a] AND MARIA FLATAU[f]

[a] *Naval Research Laboratory, Stennis Space Center, Mississippi*
[b] *SRR International, Inc., Riviera Beach, Florida*
[c] *NRC Postdoctoral Fellow, Naval Research Laboratory, Stennis Space Center, Mississippi*
[d] *Department of Civil and Environmental Engineering and Earth Sciences, University of Notre Dame, Notre Dame, Indiana*
[e] *Department of Physical Oceanography, Ocean University of Sri Lanka, Colombo, Sri Lanka*
[f] *Naval Research Laboratory, Monterey, California*

(Manuscript received 22 July 2021, in final form 30 November 2021)

ABSTRACT: Upper-ocean heat content and heat fluxes of 10–60-day intraseasonal oscillations (ISOs) were examined using high-resolution currents and hydrographic fields measured at five deep-water moorings in the central Bay of Bengal (BoB) and satellite observations as part of an international effort examining the role of the ocean on monsoon intraseasonal oscillations (MISOs) in the BoB. Currents, temperature, and salinity were sampled over the upper 600–1200 m from July 2018 to June 2019. The 10–60-day velocity ISOs of magnitudes 20–30 cm s^{-1} were observed in the upper 200 m, and temperature ISOs as large as 3°C were observed in the thermocline near 100 m. The wavelet cospectral analysis reveals multiple periods of ISOs carrying heat southward. The meridional heat-flux divergence associated with the 10–60-day band was strongest in the central BoB at depths between 40 and 100 m, where the averaged flux divergence over the observational period is as large as 10^{-7} °C s^{-1}. The vertically integrated heat-flux divergence in the upper 200 m is about 20–30 W m^{-2}, which is comparable to the annual-average net surface heat flux in the northern BoB. Correlations between the heat content over the 26°C isotherm and the outgoing longwave radiation indicate that the atmospheric forcing typically leads changes of the oceanic heat content, but in some instances, during fall–winter months, oceanic heat content leads the atmospheric convection. Our analyses suggest that ISOs play an important role in the upper-ocean heat balance by transporting heat southward, while aiding the air–sea coupling at ISO time scales.

KEYWORDS: Ocean; Indian Ocean; Currents; Eddies; Ekman pumping/transport; Fluxes; Mass fluxes/transport; Mesoscale processes; Ocean dynamics; Rossby waves; Transport; Wavelets; Wind stress; Wind stress curl; Atmosphere-ocean interaction; Eddies; Ekman pumping; Energy transport; Surface layer; Thermocline; Intraseasonal variability; Oceanic variability

1. Introduction

The atmosphere–ocean coupling plays an important role on the development of the Asian monsoon over the Bay of Bengal (BoB) (Sengupta et al. 2001; Fu and Wang 2004). The evolution of the upper-ocean heat content and mixed layer structure in response to the marine surface layer is key to the understanding of the atmosphere–ocean coupling. The sea surface temperature (SST) and upper-ocean heat content are influenced by both ocean dynamics and atmospheric surface fluxes across multiple time scales. In the following a brief description of both atmospheric and oceanic intraseasonal variability is presented before discussing the oceanic intraseasonal variability and their impacts on the air–sea coupled processes, based on observations collected during 2018–19 as part of an international effort in the BoB (Shroyer et al. 2021).

Corresponding author: Hemantha W. Wijesekera, hemantha.wijesekera@nrlssc.navy.mil

a. Monsoon intraseasonal oscillations

The Asian monsoon over the BoB is dominated by boreal summer intraseasonal oscillations (BSISOs) that propagate in all directions and have periods of 2–6 weeks. The monsoon intraseasonal oscillation (MISO) is a particular component of BSISOs, and is characterized by alternating episodes of active and suppressed atmospheric convection that slowly move northward in the eastern Indian Ocean and South China Sea during the Indian Ocean summer monsoon (e.g., Krishnamurti and Ardanuy 1980; Goswami et al. 1998; Sengupta et al. 2001; Kemball-Cook and Wang 2001; Gadgil 2003; Goswami et al. 2003; Kripalani et al. 2004). Negative/positive SST anomalies, generated by fluctuations of net heat flux at the ocean surface, move northward following regions of active and suppressed convection. While intraseasonal SST variations in this region are largely a response to atmospheric forcing, they also have important flux feedbacks onto the MISO that support its maintenance and propagation (e.g., Fu et al. 2003; Gao et al. 2019), and thus can modulate intraseasonal rainfall. Krishnamurti et al. (2017) suggest that apart from

DOI: 10.1175/JPO-D-21-0161.1

SST, oceanic heat content over the upper 40 m of depth shows a robust intraseasonal signal, which propagates northward at the rate of roughly 1° of latitude per day, with a lag of roughly 4–6 days between the appearance of this signal in the surface wind speed and following heat-content anomaly. Such coherent evolution of SST, near-surface heat content, and convection indicates that air–sea interactions are important to the maintenance of the MISO (e.g., Sengupta et al. 2001; Krishnamurti et al. 2017). The importance of the MISO in the predictability of the Asian monsoon has been well documented (Fu et al. 2003, 2007; Flatau et al. 2003) and includes the upscale feedback of subseasonal oscillations onto the seasonal cycle of precipitation in the region.

The general view of atmosphere–ocean interactions within MISO is that the surface latent heat flux is critical for the positive SST anomalies (Sengupta et al. 2001). Based on coupled model simulations, Fu and Wang (2004) suggest that intraseasonal SST is a result of atmospheric convection, but at the same time, positively feeds back to the atmosphere. Zhou and Murtugudde (2014) examined the development of the MISO, and found that, during most years, the atmosphere drives the ocean and plays an active role in the ocean–atmosphere interactions during the northward-propagating MISO, similar to the general view (Sengupta et al. 2001; Fu et al. 2003; Fu and Wang 2004). However, in certain instances, ocean dynamics (mainly the meridional heat transport) lead to warm SST anomalies, which propagate northward from ~5° to ~15°N along the 85°–90°E longitudinal band. These instances demonstrate the active role that the ocean can play in generating the warm SST anomalies that enhance air–sea interactions during the MISO.

b. Oceanic intraseasonal oscillations

Like in the atmosphere, strong oceanic intraseasonal oscillations (ISOs) in the BoB have been reported from analyses of satellite-derived sea surface height anomalies (SSHAs), mooring temperature and velocity records, and model output (Hacker et al. 1998; Babu et al. 2003; Sengupta et al. 2004; Prasanna Kumar et al. 2004; Goswami 2005; Miyama et al. 2006; Kurien et al. 2010; Girishkumar et al. 2011, 2013; Chen et al. 2018; Cheng et al. 2013; Vidya and Prasanna Kumar 2013; Dandapat and Chakraborty 2016; Wijesekera et al. 2016; Cheng et al. 2018; Pirro et al. 2020a). Girishkumar et al. (2013) examined moored temperature records in the BoB at 8°, 12°, and 15°N along 90°E, and reported 30–120-day time scales for ISOs in the thermocline region at three distinct periods of 30–70 days, near 90 days, and near 120 days. They suggest that large-amplitude ISOs near 90- and 120-day variabilities are generated remotely by intraseasonal winds from the equatorial Indian Ocean and the eastern BoB. They further conclude that the 30–70-day ISOs (i.e., those with comparable periods to the atmospheric MISO) can be impacted by local Ekman pumping, but both zonal winds in the equatorial Indian Ocean and alongshore winds in the eastern BoB appear to be major forcing mechanisms. Their study suggests that the thermocline depth in the central BoB is significantly modulated by Rossby waves propagating from the eastern boundaries (e.g., Andaman and Nicobar Islands) where equatorial Kelvin waves impact the circulation and eddy activities in the Andaman Sea and the BoB (Chatterjee et al. 2017).

Previous work has shown that remote forcing in the Bay of Bengal is linked to Kelvin waves, driven by equatorial intraseasonal winds, which propagate eastward along the equator during April/May and September/October (e.g., Wyrtki 1973). Upon reaching the eastern boundary, the energy of the Kelvin waves is reflected back in part as long Rossby waves, and reaches the central-eastern BoB during July–August (Han et al. 1999, 2001; Han 2005; Nagura and McPhaden 2010). The remaining energy is partitioned into two coastally trapped Kelvin waves traveling poleward (Moore 1968; Chen et al. 2018). Westward propagating waves/eddy-like features have been identified from moored observations in the south-central BoB (Wijesekera et al. 2016; Pirro et al. 2020a,b) where they are known to modulate currents in the Bay of Bengal. For example, Pirro et al. (2020a) discussed the interactions between 30- and 60-day summertime ISOs and the Southwest Monsoon Current (also known as the Summer Monsoon Current) in the southern BoB. Their analysis suggests that meridional momentum and heat-flux divergences associated with ISOs have a significant impact on mean currents and temperatures in the southern BoB.

Cheng et al. (2013) examined intraseasonal oscillations of SSH over the BoB using altimetry data and an eddy-resolving ocean model. They noted strong seasonality of these SSH-based ISO signals. Large-amplitude ISOs were found along the eastern and northern coasts of the BoB, in the western BoB, and in a zonal band across the BoB centered near 5°N. The annual maxima amplitudes of ISOs in the western BoB occur in spring, and during summer and fall for the ISOs southeast of Sri Lanka. The latter are consistent with the timing of Rossby-wave reflection by Kelvin waves in the eastern Indian Ocean previously discussed. Model simulations show high eddy energy in the western BoB due to the barotropic/baroclinic instability of the East India Coastal Current (Chen et al. 2018; Cheng et al. 2013; Kurien et al. 2010). Cheng et al. (2013) further suggested two southwest-directed eddy pathways in the BoB: one located near the western boundary and the other in the central BoB (referred as the central pathway). By combining satellite SSH and numerical simulations, Cheng et al. (2018) noted that when coastal-trapped downwelling (upwelling) Kelvin waves propagate to the tip of the Irrawaddy Delta off Myanmar, anticyclonic (cyclonic) eddies are generated there that subsequently propagate southwestward (i.e., the central pathway), thus contributing to high intraseasonal variability in the central BoB. Gordon et al. (2017) observed an intrathermocline anticyclonic eddy with water characteristics of the Andaman Sea that was located in the central BoB, further evidencing the central pathway of eddy propagation. This study also demonstrated the role such eddies have in the transport of varying water masses across the Bay of Bengal.

c. BoB field program and objectives

For the purpose of examining atmosphere–ocean processes during MISO events, the U.S. Office of Naval Research (ONR) sponsored a coordinated international program, titled

Oceanic Control of Monsoon Intraseasonal Oscillations in the Tropical Indian Ocean and the Bay of Bengal (MISOBOB) (Shroyer et al. 2021). As part of this international effort, the U.S. Naval Research Laboratory (NRL) conducted a research program, Role of Indian Ocean on Monsoon Intraseasonal Oscillations (RIO-MISO), which includes both atmosphere and ocean measurements along with coupled ocean–atmosphere modeling studies. As part of the joint program, five deep-water moorings were deployed in the central BoB, along with two multiday ship surveys in July 2018 and June 2019. These observations encompass two monsoon periods. The 2018 monsoon season (June–September) is identified as a below-normal monsoon season, with the rainfall over India about 91% of the long-period average (https://reliefweb.int/report/india/india-meteorological-department-end-season-report-2018-southwest-monsoon), whereas the 2019 monsoon produced unusually high rainfall over India. The 2019 monsoon season was delayed, with weak convective spells that lasted until late June, and the season extended later than normal into October (Gadgil et al. 2019). It has been suggested that the strong positive Indian Ocean dipole generated anomalously dry June and extremely wet September (Ratna et al. 2021).

The main objective of this study is to evaluate intraseasonal variability of currents, temperature, heat fluxes, and upper-ocean heat content quantitatively, and to examine the importance of eddy heat transports on the upper-ocean heat balance. The secondary objective is to explore connections between oceanic heat content in a near-surface layer and atmospheric convection. The variability of ocean heat content at ISO time scales is likely controlled by both the atmospheric forcing associated with MISO events, and the dynamics of oceanic eddies and planetary waves. Therefore all of these processes are needed to evaluate the ocean's role on MISO at ISO time scales.

The paper is organized as follows: instrumentation and datasets from moorings are described in section 2, along with satellite data, and meteorological data from ERA5 model output and Research Moored Array for African–Asian–Australian Monsoon Analysis and Prediction (RAMA) buoy winds. Background winds and net surface heat fluxes from ERA5 model output, and RAMA buoy winds, and SST and outgoing longwave radiation (OLR) from satellite products are described in section 3. Seasonal variability of currents, transports, and temperature from moored observations are presented in section 4. In section 5, multiple time-scale features (such as 10–60-day ISOs) are identified using wavelet techniques. In section 6, ISO fluxes of heat are presented from both wavelet and traditional covariance methods. Discussions of local/remote forcing aspects of ISOs, meridional heat-flux divergence, and plausible connections between heat content and atmospheric variability such as OLR are given in section 7. Summary and conclusions of this study are presented in section 8.

2. Instrumentation and data

a. Moorings

Five moorings containing acoustic Doppler current profilers (ADCPs) and a variety of temperature, conductivity, and microstructure sensors were deployed in the western BoB from July 2018 to June 2019 at water depths ranging from about 3000 m to over 3800 m (Fig. 1). Four of the moorings were deployed along a north–south line along 85.75°E, at approximately every 2 degrees of latitude from 8° to 14°N. A fifth mooring was deployed at approximately 2° of longitude west of N1, about 200 n mi (≈370 km) from the coast of Sri Lanka. Mooring positions, start and end times, ADCP profile range, water depths, numbers and type of ADCPs and TCP (temperature, conductivity, pressure) sensors, and inertial periods are provided in Table 1. These moorings were designed to measure currents and hydrography from near the surface down to depths of about 1300 m.

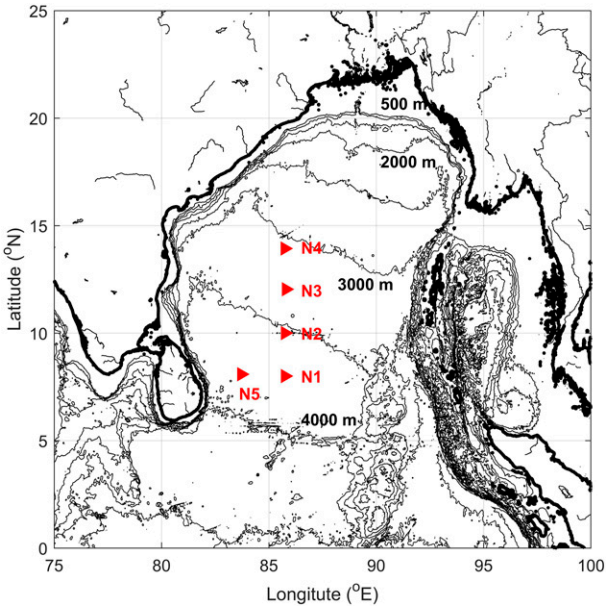

FIG. 1. Bathymetric map of the BoB. Locations of the moorings are marked by red triangles. Thin lines are isobaths ranging from 500 to 5000 m with contour intervals of 500 m. Only 500-, 2000-, 3000-, and 4000-m isobaths are marked.

There were two configurations for the moorings. Moorings N1 and N5 made measurements to nearly 1300 m (Table 1) and contained a five-head 300-kHz Sentinel-V100 ADCP mounted in an elliptical-shaped ball at depths of approximately 90 and 110 m, respectively. A MicroMoor microstructure package was placed on the mooring line below the five-head ADCP at approximately at 115 m (N1) and 135 m (N5). Note that the MicroMoors (developed by Rockland Scientific, Inc.; Lueck et al. 2015) which provided measurements of turbulent mixing are not discussed in this paper but are presented in Luecke et al. (2021). Moorings N1 and N5 also contained an upward-looking Teledyne RD Instruments Workhorse ADCP, operating at 300 kHz, and a downward-looking Teledyne RD Instruments Long Ranger ADCP, operating at 75 kHz, that were mounted, below the five-head ADCP and MicroMoor, in a Flotation Technology buoy, 45 in. in diameter, at a depths of about 131 m (N1) and 158 m (N5), and a second Flotation Technology buoy with a

TABLE 1. Mooring summary. Locations of the moorings (N1–N5) are given along with geographical location, start time, end time, top depth of ADCP velocity profile (Z1), bottom depth of profile (Z2), water depth (Depth), and inertial period (IP). The last three columns show groupings of ADCPs (300- and 75-kHz ADCPs), TCP, TC (SBE37), and TP (SBE39) sensors, and thermistors (SBE56, Vemco, RBR). Note: the locations are anchor dropped position recorded by the ship.

Site	Lat (°N)	Lon (°E)	Start 2018 (m day^{-1})	End 2019 (m day^{-1})	Z1 (m)	Z2 (m)	Depth (m)	IP (days)	ADCP 300 kH, 75 kHz	SBE37 (TCP,TC), SBE39 (TP)	SBE56, Vemco, RBR
N1	8.002	85.753	11 Jul	29 May	16	1288	3741	3.592	2, 2	11, 1, 2	11, 16, 5
N2	10.003	85.753	12 Jul	30 May	16	616	5313	2.878	1, 1	8, 0, 2	11, 15, 4
N3	12.034	85.798	11 Jul	31 May	16	616	3292	2.397	1, 1	6, 1, 5	8, 14, 4
N4	13.945	85.742	11 Jul	30 May	16	592	3081	2.075	1, 1	9, 0, 6	9, 13, 4
N5	8.085	83.718	Jul 15	13 Jul	32	1272	3815	3.555	2, 2	10, 5, 5	9, 14, 3

downward-looking 75-kHz ADCP at depths of 740 m (N1) and 770 m (N5). Moorings N2–N4 made measurements to about 600 m. Moorings N2 and N3 contained an upward-looking five-head Sentinel-V100 ADCP and a downward-looking 75-kHz Long Ranger ADCP, mounted in a Flotation Technology buoy, at depths of about 75 m (N2) and 100 m (N3). Mooring N4 was similarly equipped compared to N2 and N3 but contained an upward looking Workhorse ADCP mounted with the Long Ranger at 75 m.

Current profiles for most of the analyses ranged from approximately 16 m below the surface to depths of nearly 1300 m over the full recording period. Some velocities were measured to within about 5 m of the surface for parts of the recording period. Currents were sampled every hour by the Long Ranger and Workhorse, and Sentinel ADCPs. The five-head Sentinel ADCPs also sampled at 1 Hz for 15 min every 3 h in order to measure waves. Vertical depth resolutions for the current measurements were 8 m for the Long Ranger and 2 m for the Workhorse and Sentinel ADCPs. The accuracy of the Sentinel V100 and Workhorse are 0.5% of the water velocity $\pm$ 0.5 cm s^{-1}. The accuracy of the Long Ranger is 1% of the water velocity.

All of the moorings were subjected to motions at semidiurnal tidal frequencies which were enhanced during strong current flows. Pressure records for each mooring show tidally induced dips of a meter or two throughout the deployment. Larger excursions from the minimum buoy depth that ranged from about 10–30 m commonly occurred at the moorings throughout the measurement period. The mooring motion was further complicated by fishing activity since the ADCP balls nearest the surface were often entangled with fishing gear. Four, two, and three temperature and conductivity sensors were lost due to breakage of the top 40, 5, and 10 m of rope near the surface at N1, N2, and N4, respectively.

Full data records were returned at each mooring from the 75-kHz ADCPs for the deeper water column. In the upper 100 m, the data recording from the Sentinel V100 ADCPs stopped in the last 2–3 months of the deployment period due to battery expiration. In general data quality was good. However, some data segments required editing. Single data spikes were first removed and interpolated. Bad data spanning 4 h or less were removed and then interpolated in time to fill the gaps. Bad data spanning more than 4 h were flagged as bad. Some of the shallowest bins close to the surface, where more than 25% of the data were bad, were dropped. These quality-controlled velocity records were gridded using the pressure data and interpolated to common depth levels among the moorings. Many of the analyses here use velocity data that are at 8-m levels.

Time series of the east–west velocity component (U) and the north–south velocity component (V) at hourly resolution as a function of depth are shown for each mooring in Fig. 2. Positive U and V velocity values are eastward and northward, respectively. The vertical streaking in the velocities is due to near-inertial currents which have periods at the moorings greater than 36 h (Table 1). Figure 2 displays several distinct low-frequency flow patterns: (i) strong surface currents in the upper 200 m especially during monsoon periods, (ii) intraseasonal oscillations (~30-day period) extending all the way to 1000 m, and (iii) deep currents of about 0.2–0.3 m s^{-1} at N5 at 800–1200-m depths during May/June 2019. Furthermore, subsurface (150–250 m) intensified currents, lasting about a month were observed at N1 and N4 during October 2018.

Each mooring also contained an assortment of sensors mounted along the line to measure temperature (T), conductivity (C), pressure (P), and dissolved oxygen (DO). There were MicroCats, Vemco, Star Oddi, RBRsolo, and RBRduo instruments. Synthetic rope with weak links, placed at the top of the mooring lines, was used to extend an instrument string to a small ball at or near the surface. MicroCats manufactured by Sea-Bird Electronics (SBE) consisted of SBE37, SBE39, and SBE56 instruments, both with and without pressure, recorded temperature and conductivity. SBE sensors provided complete records of T, C, and P. Most of the Star Oddi sensors, which measure T, C, and P, deployed in the upper 50 m on the flexible rope above the top ADCP ball were fouled, and were not used here. RBRduo sensors measured both temperature and oxygen, but oxygen measurements were limited due to fouling of sensors. Vemco sensors recorded temperature throughout the deployment period, but the resolution was limited to about 0.1°C. Sampling rates were 1 min for the Vemco and RBR recorders and 10 min for the other recorders. Groupings of hydrographic sensors used in each mooring are given Table 1. The typical spacing between sensors above 90, 100–200, 200–300, and below 300 m were 5–10, 10, 20, and 50–100 m, respectively. These sensors were unevenly spaced

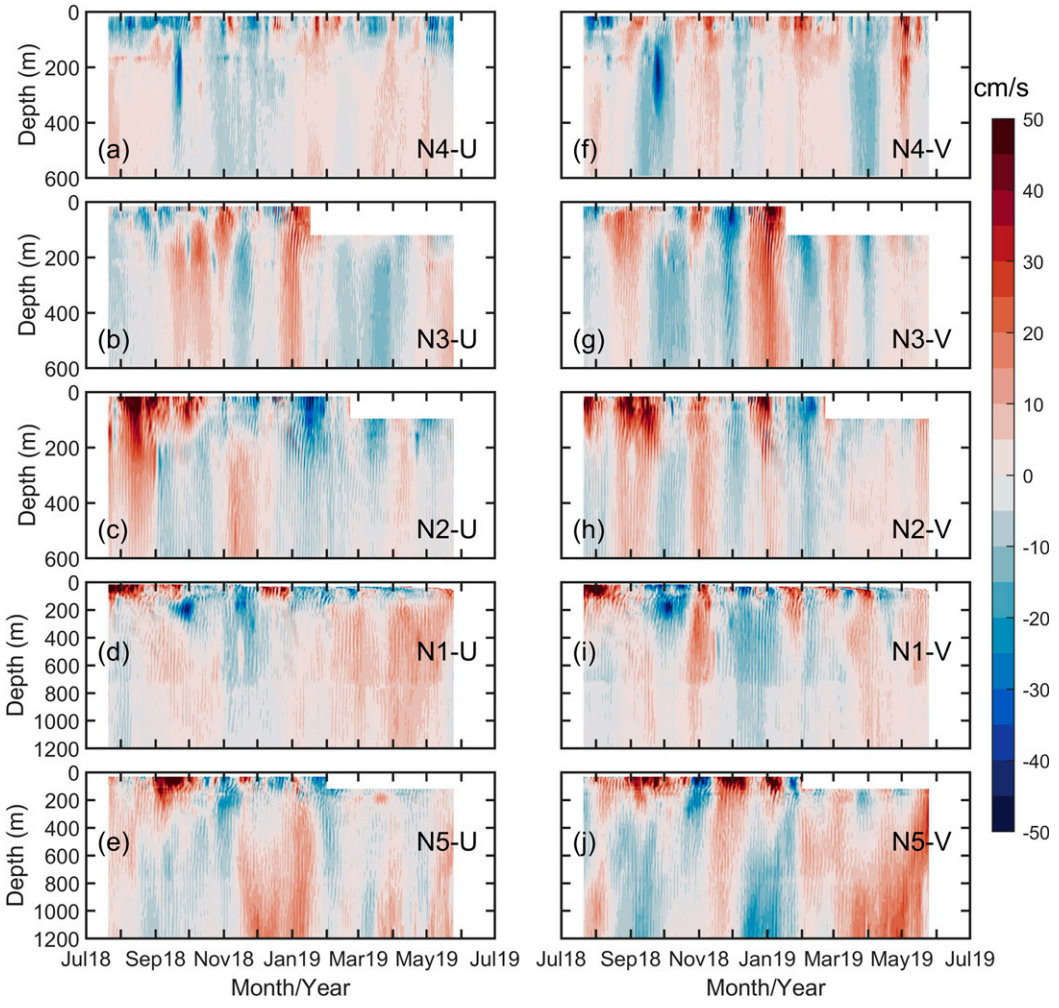

FIG. 2. Zonal (U) and meridional (V) time series at hourly and 8-m vertical resolution. White areas are areas with no data.

but were more numerous in the upper water column where strong stratification was expected. The depths of the sensors attached to the mooring lines were evaluated by interpolating the pressure records of the ADCPs and temperature/conductivity sensors in conjunction with their known location on the mooring line. The temperatures were then gridded at 4-m depth intervals. Salinities were limited to 6–11 sensors at each mooring (Table 1) and were not interpolated vertically. Salinity data were edited to remove salinity spikes and bad segments. Time–depth sections of hourly-averaged temperature for each mooring site are shown in Figs. 3a–e. Enlarged views of temperature–depth sections shown in Figs. 3f–j display large intraseasonal variability in the main thermocline near 100 m. The isothermal displacements in the thermocline were largest at N5, where a cyclonic eddy [i.e., Sri Lanka Dome (SLD)] and an anticyclonic eddy passed through the mooring site in summer and fall.

b. Satellite data products (SST, SSH, OLR)

Data products from multiple satellites were used to examine spatial and temporal variability of surface oceanographic fields and OLR from Earth and its atmosphere. The sea surface height (SSH) and associated geostrophic velocities were obtained from AVISO global SSH products (gridded sea level heights and derived variables from https://www.aviso.altimetry.fr/en/data/products/sea-surface-height-products/global.html; product user manual, https://resources.marine.copernicus.eu/documents/PUM/CMEMS-SL-PUM-008-032-062.pdf). Daily maps of SST were acquired from the NOAA high-resolution blended analysis of daily SST with 0.25° spatial resolution (https://psl.noaa.gov/). Daily maps of OLR with 1° × 1° spatial resolution were obtained from the new Climate Data Record (CDR) developed by NOAA and the University of Maryland, and these datasets can be accessed from https://climatedataguide.ucar.edu/climate-data/outgoing-longwave-radiation-olr-hirs.

c. ECMWF reanalysis (ERA5) products and RAMA buoy winds

Surface heat flux and wind observations were not available along the mooring array, during our observation period, and therefore, the European Centre for Medium-Range Weather

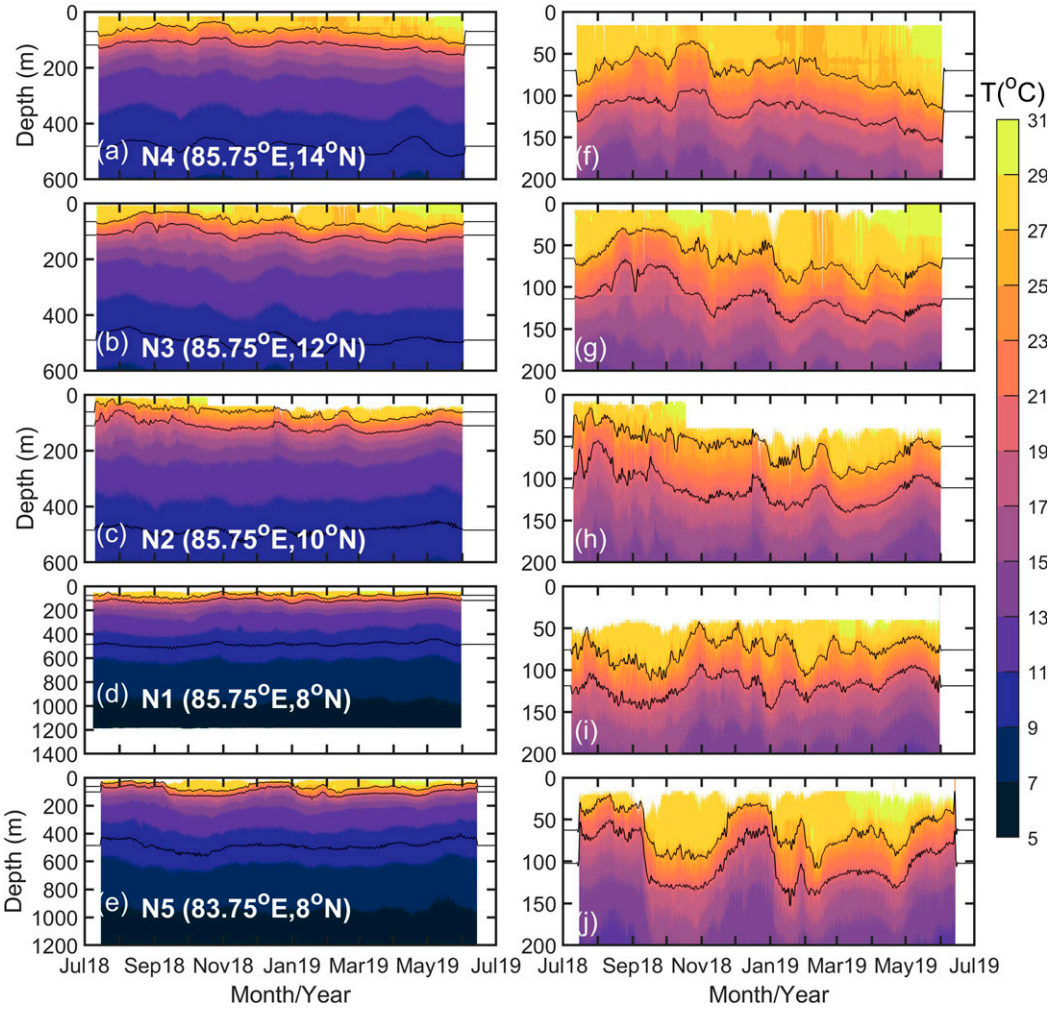

FIG. 3. Time–depth sections of hourly-averaged temperature at N1–N5. The right panels display an enlarged view of temperature variability in the thermocline. The black lines are 2-day low-passed (detided) isotherms of 10°, 20°, and 26°C. Only 20° and 26°C isotherms are marked in the right panels. Approximate locations of moorings are given in parentheses.

Forecasts (ECMWF) Reanalysis V5 (ERA5) (https://www.ecmwf.int/en/forecasts/datasets/reanalysis-datasets/era5) products were used to estimate surface stresses and surface heat fluxes including net surface shortwave flux, net surface longwave flux, latent heat flux, and sensible heat flux for the period between January 2018 and December 2019. In the following we used hourly ERA5 fluxes and wind stress with 1/4° spatial resolution.

We also used daily-averaged wind speed and direction measured at 4 m above the surface from the RAMA mooring array (McPhaden et al. 2009) at 90°E, 12°N and 15°N. There are large gaps in the 2-yr records, and therefore meteorological information from both buoys is used to obtain a general view of wind forcing in the BoB. These datasets are available at https://www.pmel.noaa.gov/tao/drupal/disdel/.

3. Background meteorology

Figure 4 shows time–latitude plots of longitudinally averaged (84°–90°E) ERA5 surface wind stress components (τ_x, τ_y) at 10 m above the sea surface, wind stress curl ($\nabla\times\boldsymbol{\tau}$), and satellite SST and OLR for the 2018/19 monsoon seasons, where $\boldsymbol{\tau}$ is the wind stress vector. These variables were roughly uniform longitudinally in the central part of the BoB owing to the predominantly east–west orientation of the MISO, and here, we used variables averaged between 84° and 90°E.

Figure 5 shows time series of wind stress magnitude and direction, net surface heat flux (Qnet), and OLR at N3 (12°N, 85.75°E) along with wind stress and direction estimated from RAMA buoy observations at 12°N, 90°E, and 15°N, 90°E. Only partial wind records were found at most of the RAMA

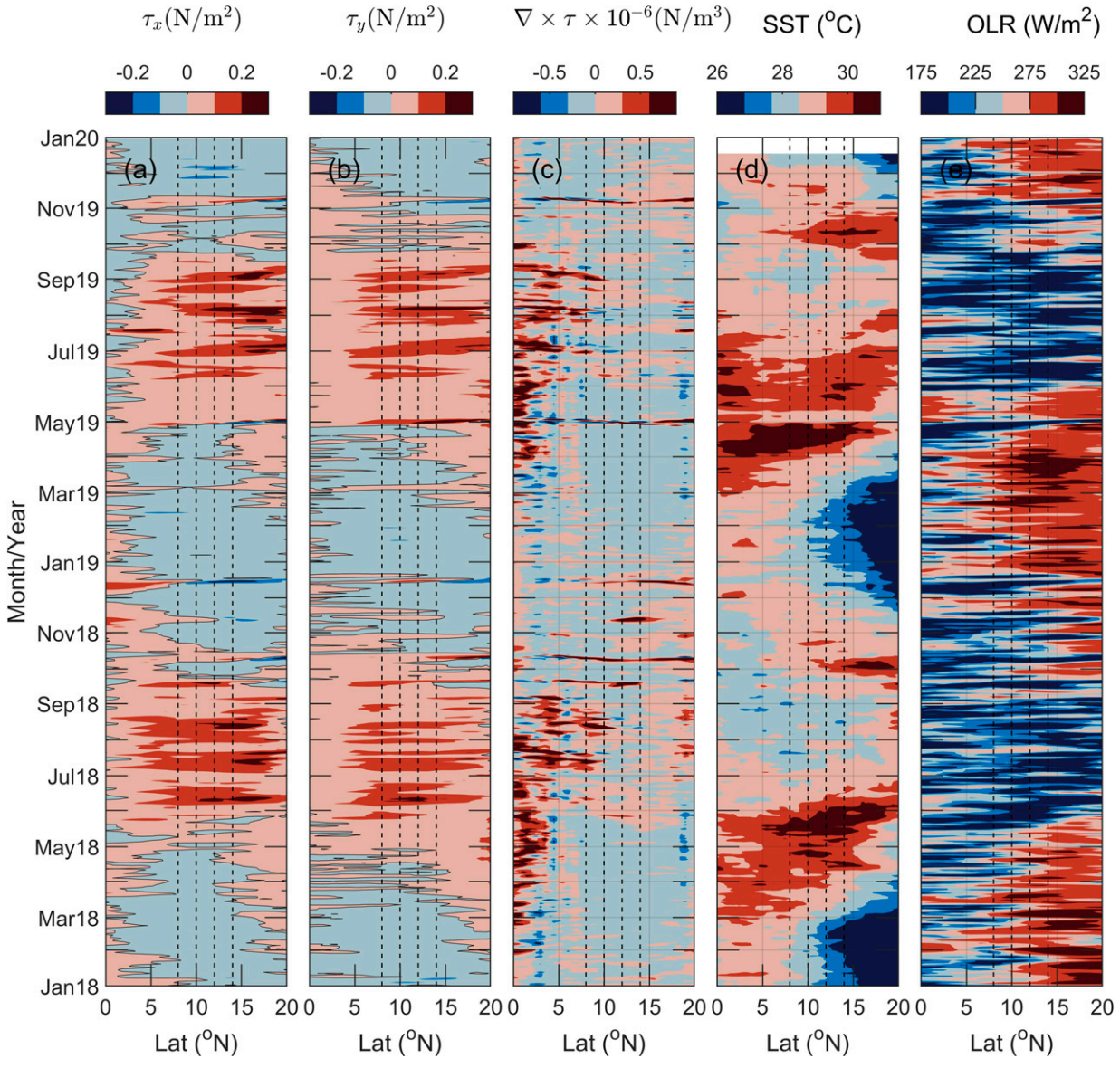

FIG. 4. (a) Latitude–time plot of longitudinally averaged (between 84° and 90°E) surface zonal stress (τ_x), (b) meridional stress (τ_y), and (c) wind stress curl ($\nabla \times \boldsymbol{\tau}$) from ERA5 reanalysis products from https://www.ecmwf.int/en/forecasts/datasets/reanalysis-datasets/era5, (d) SST from https://psl.noaa.gov/, and (e) OLR from the Climate Data Record (CDR), https://climatedataguide.ucar.edu/climate-data/outgoing-longwave-radiation-olr-hirs. Plots were constructed from daily averaged wind stress, SST, and OLR. Thin black lines in (a) and (b) represent zero stress contours. Vertical dashed lines are the meridional positions of NRL moorings.

sites, and here we combined 12° and 15°N sites to obtain a continuous record for 2018/2019. Even though RAMA buoys are situated more than 500 km away from the NRL moorings, wind stress magnitudes and directions are similar (Figs. 5a,b). Note that wind speeds and directions from RAMA buoys were measured at 4 m above the surface, which were converted to 10-m wind stress using the drag formulation given in Hwang (2011) for neutral stability conditions. Figures 4 and 5 display summer monsoon winds consisting of three to four short pulses, each lasting about 10–30 days. These wind events are characterized by northward propagating component with speeds of 3°–4° day^{-1} (Figs. 4a,b), where the slope of the time–latitude plot of wind stress is the northward propagation speed. The speed of propagation is faster than the typical speed of 1°–1.5° day^{-1} of 20–100-day filtered precipitation anomalies (e.g., Sharmila et al. 2013). In 2018, the first BSISO reached the BoB from late May to early June, while in 2019, a strong BSISO arrived from middle to late June indicating a delay of the 2019 summer monsoon. Wind stress curl also shows 10–30-day fluctuations embedded within the seasonal cycle (Fig. 4c), and was strongest at lower latitudes (<10°N). The wind stress curl can impact ocean circulation through

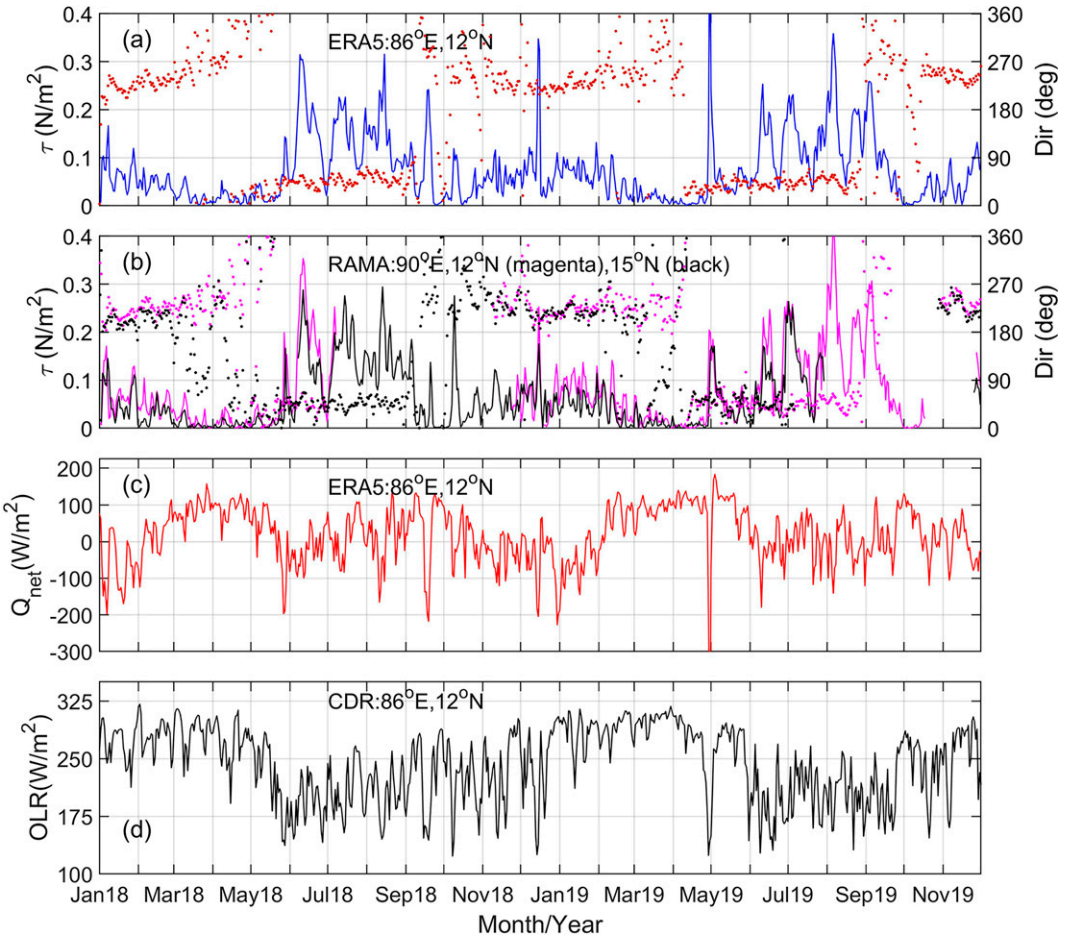

FIG. 5. (a) Time series of daily averaged surface wind stress magnitude (τ) (blue line) and direction (Dir) (red dots) at 12°N, 85.75°E (N3 site) from ERA5 model output. (b) Daily averaged wind stress (solid lines) and direction (dots) at 12° and 15°N, 90°E from RAMA buoy measurements, where magenta and black colors represent 12° and 15°N, respectively. Buoy measurements at 12° and 15°N were combined to construct a 2-yr time series. (c) Daily averaged net surface heat flux (Q_{net}) at 12°N, 86°E from ERA5 model output. (d) Daily averaged outgoing longwave radiation (OLR) at 12°N, 86°E from CDR developed by NOAA and University of Maryland. Here the direction of the wind is where the wind is originating, downward net heat flux is positive, and the OLR (upward flux) is positive.

Ekman pumping and these aspects are examined in the discussion.

As shown Figs. 4d, 4e, and 5d both SST and OLR vary seasonally. Warming begins near the equator in March, and the warming trend gradually propagates northward. The SST in the middle of the BoB reaches ~31°C in May 2018 (Fig. 4d), while the central BoB receives net surface heating of about 100 W m^{-2} (Fig. 5c) with OLR of 300 W m^{-2} (Fig. 5d). In some years, the premonsoon warming is disrupted by cyclones moving from the south, as observed during the passage of Cyclone Fani in late April–early May 2019 (Mohanty et al. 2020). The surface cooling dominates during the onset of the monsoon, while for the rest of the summer monsoon, heating and cooling events prevailed with changing winds (Figs. 4 and 5). Shroyer et al. (2021) discussed the 2018 monsoon onset, and noted an active phase during 4–13 June with a net surface cooling of 69 W m^{-2}, and a break phase on 14–18 June with a net surface heating of 83 W m^{-2} near 15°N, 90°E. The summer monsoon characterizes with low OLR with synoptic to intraseasonal fluctuations (Figs. 4e, 5d). Prominent intraseasonal variations of SST are difficult to observe in unfiltered data, (Fig. 4d), but intraseasonal variations of OLR are much more apparent, especially during fall/winter (Figs. 4e, 5d). The winter monsoon period (November–February) can be characterized as a period of weak northeasterly winds (approximately one-third of the magnitude of summer winds) with negligible averaged net surface heat flux (based on ERA5 output), distinct intraseasonal fluctuations of OLR, and drop in SST by 2°–4°C when compared to premonsoon conditions during May, and high OLR over the BoB.

The ERA5 net heat flux averaged for the observational period (June 2018–June 2019) and for the period between January 2018 and December 2019 along the mooring array (N1–N4) are about 27 and 20 W m^{-2}, respectively, with a

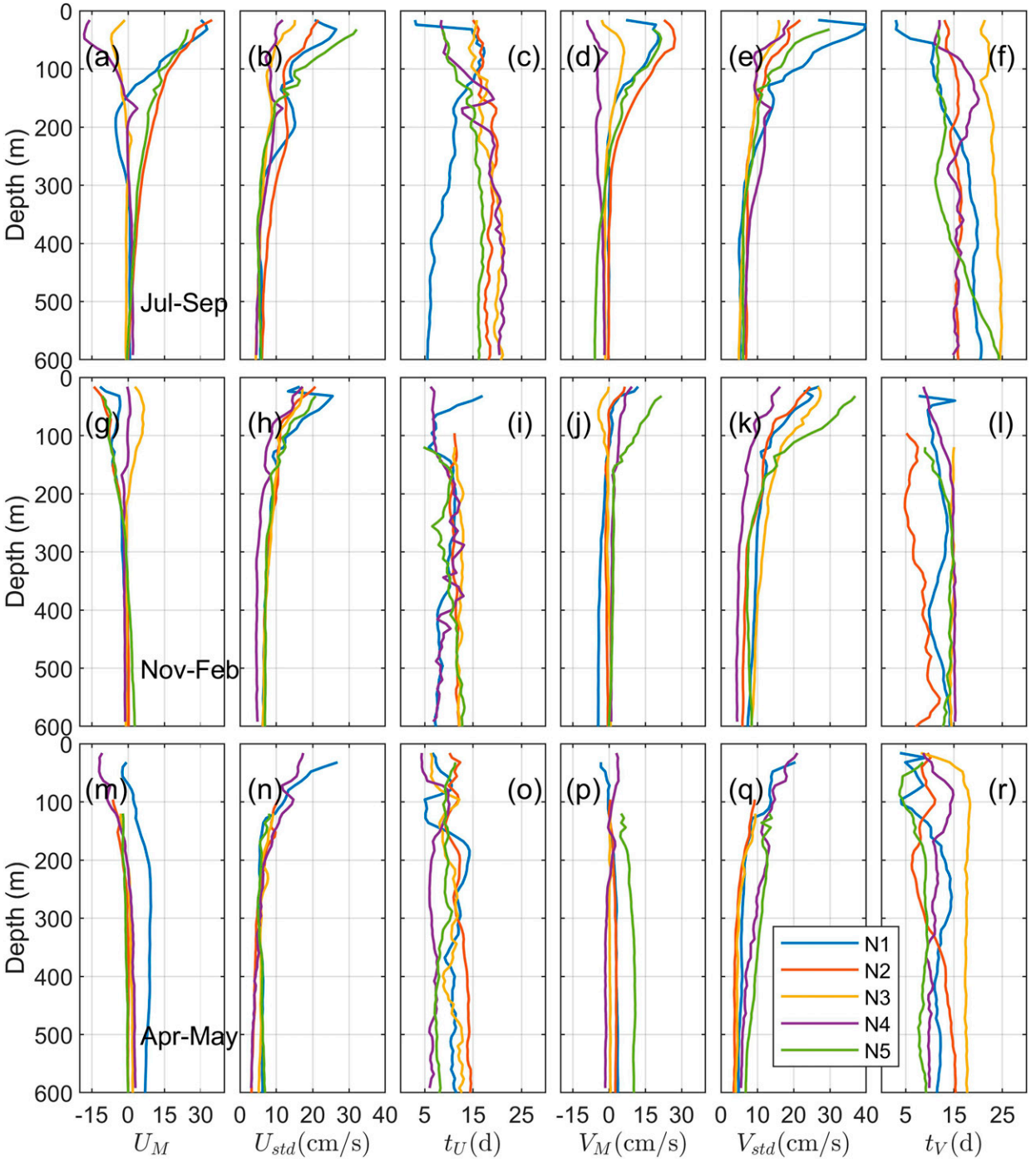

FIG. 6. Profiles of seasonally averaged currents (U_M, V_M), standard deviations (U_{std}, V_{std}), and decorrelation time scales for 4-day low-pass-filtered U and V (t_U and t_V), representing (a)–(f) summer monsoon (July–September), (g)–(l) winter monsoon (November–December), and (m)–(r) presummer monsoon (April–May).

standard deviation of 290 W m^{-2} and a standard error of 2 W m^{-2} for hourly estimates. However, several investigators reported large uncertainties and biases of ERA-Interim surface heat fluxes, especially at intraseasonal time scales (Sanchez-Franks et al. 2018; Yu et al. 2007). Therefore, net surface heat fluxes from ERA5 were compared with the meteorological observations discussed by Weller et al. (2019) in the northern BoB near 18°N, 89.5°E. Weller et al. (2019) report that the annual-averaged net surface heat flux for 2015 is about 37 W m^{-2}. The annual-averaged ERA5 net heat flux

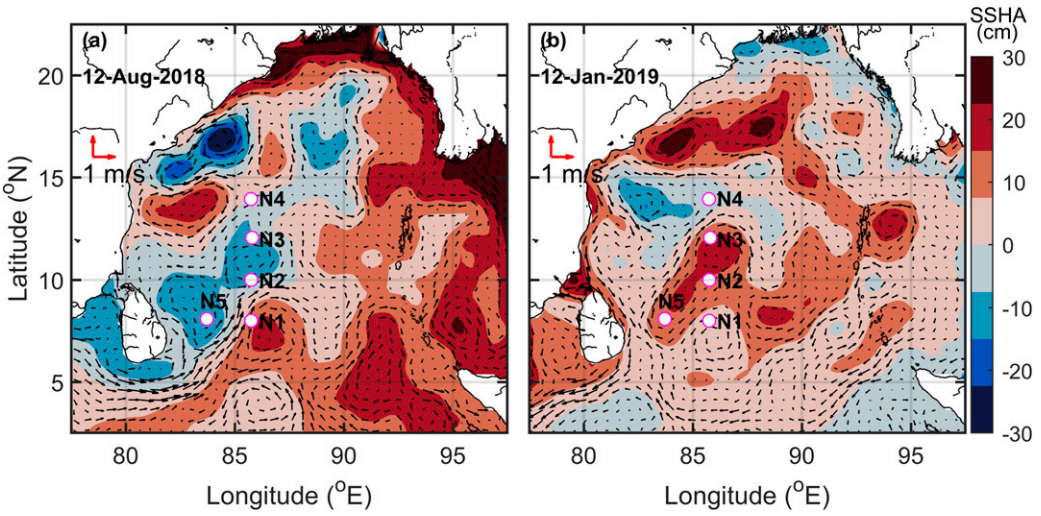

FIG. 7. AVISO SSHA on (a) 12 Aug 2018 and (b) 12 Jan 2019 along with geostrophic current vectors. Solid white circles are the NRL mooring sites.

for 2015 is 12 W m^{-2}, indicating that the ERA5 estimate, on annual average, can be biased low by 20 W m^{-2}. Weller et al. (2019) further report seasonal differences in wind direction and the humidity of the air, in cloud cover, and in the occurrence of intraseasonal oscillations. The northern bay received largest heat gain during spring intermonsoon, while the summer monsoon was dominated by strong rains and wind forcing events, with little mean heat gain. They further mentioned that the fall intermonsoon was transitional, starting with intraseasonal variability accompanied by heat and freshwater gain and the strongest oceanic heat loss during the winter monsoon.

4. Seasonal variability

a. Currents and transports

Profiles of seasonally averaged currents (U_M, V_M) and the associated standard deviations (U_{std}, V_{std}) representing the summer monsoon (July–September 2018), winter monsoon (November 2018–February 2019), and presummer monsoon (April–May 2019) are illustrated in Fig. 6. Note that 4-day low-pass-filtered currents were used to examine seasonal variability. During the summer of 2018, mean currents in the upper 100 m at N1–N4 (8°–10°N, ~85.75°E) were toward the northeast at about 30 cm s^{-1} (Figs. 6a,d), but hourly velocities in September were as large as 125 cm s^{-1} as observed at N5 (8°N, ~83.7°E). The standard deviations of seasonal currents in the upper 200-m layer were either comparable or larger than the mean indicating strong subseasonal variability (Figs. 6a–k), especially during summer and winter monsoons. The lower layer between 200 and 600 m, the mean currents were less than 5 cm s^{-1} and fluctuations were 5–10 cm s^{-1}, indicating that the subseasonal variability dominated in the deeper part of the water column. During the premonsoon period both seasonal means and fluctuations were smaller compared to the summer season (Figs. 6m–r). A longitude–latitude map of SSHA on 12 January 2019 (Fig. 7b) displays weak currents and several eddies, with some passing through the NRL mooring array (see also section 5).

The moorings N1, N2, and N5 captured the seasonally varying Summer Monsoon Current (SMC) SLD, and a large anticyclonic eddy (Fig. 7a). During the summer monsoon, the eastward flowing SMC south of Sri Lanka entered the southern BoB and turned northeastward while passing between N1 and N5, and then moved eastward between N1 and N2 (Fig. 7a). Here the SMC was captured twice by the triangular mooring setup, N5–N1–N2. The maximum eastward flow at N2 occurred during the middle of October (Fig. 2) as the SMC passed between N1 and N2. The average northward transport between N1 and N5 in the upper 200 m for the 90-day period (15 July–15 October) is about 3.7 Sv (1 Sv ≡ 10^6 m^3 s^{-1}), and the average eastward transport between N1 and N2, is about 5.5 Sv, where volume transport was estimated as a product of mean velocity × thickness of the layer × distance between the two moorings considered. Similarly northward and eastward transports above 600 m are 5.6 and 6.3 Sv, respectively, which in turn implies that the lower layer (200–600 m) transport during later summer is less than 1 Sv.

The pattern of the SMC during July–September has similarities with previous observations made in the southern BoB (Wijesekera et al. 2016; Webber et al. 2018). For example, the SMC strength and position are driven by the combination of local forcing (wind stress curl over the SLD) and remote equatorial forcing (Kelvin and Rossby wave propagation). The estimate of northward transport during the summer of 2014 is about 8 Sv over a 50-day period (Wijesekera et al. 2016), which is roughly comparable to the present estimate of the SMC transport [i.e., (5.6 + 6.3)/2 ~ 6 Sv] during the summer of 2018 for a 90-day period. Webber et al. (2018) report that the SMC transport during July 2016 was 16–24 Sv. Their estimate is much larger than the estimate reported by

Wijesekera et al. (2016) and the current estimate. Webber et al. (2018) noted that up to 2/3 of their estimate is associated with recirculating eddies, including the Sri Lanka Dome.

b. Integral time scales

These subseasonal oscillations may contain mesoscale eddies and planetary wave motions. To get a dynamically measured quantity of temporal persistence, the integral time scale of currents was examined. The integral time scale of a variable is estimated using the time-lagged autocorrelation coefficient of the longitudinal velocity component (e.g., Tennekes and Lumley 1972). Here, integral time scales were computed from the 4-day low-passed U and V for each mooring over the summer monsoon, winter monsoon, and premonsoon periods. Profiles of decorrelation time scales, t_U and t_V for U and V, respectively show variations with direction of the flow, depth, and seasonality (Fig. 6, columns 3 and 6). Integral time scales generally ranged from about 5–15 days in the upper 100 m for most of the sites. Below 100 m, both t_U and t_V are nearly independent with depth, except at southern moorings N1 (Fig. 6c) and N5 (Fig. 6f) during summer. The decorrelation time scale t_U is largest during summer compared to winter and spring, while t_V has a wide range of values with largest at N3 close to 25 days during summer monsoon. These differences in integral time scales at different mooring sites reflect fundamental temporal scales of variability in the underlying oceanic flow with the existence of multiscale ISOs (more details in section 5).

c. Temperature

Figure 8 displays seasonal mean temperatures, temperature differences between the seasonal mean and the mean over the observational period (which is close to annual mean), and standard deviations of temperature at mooring sites. Mean temperatures in the upper 75 m at all the mooring sites are roughly similar, indicating less spatial variability of temperature (Figs. 8a–c and 4d), but there was considerable variability in the thermocline between 75 and 300 m, especially during 2018 summer and 2019 premonsoon periods (Figs. 8a,c). Spatial variability of temperature in the thermocline was small during winter (Fig. 8b). The seasonal variability of temperature shows a dramatic change in the thermocline near 100 m (Figs. 8d–f), where the temperature change from premonsoon to summer/winter can be as large as 3°–6°C. During the premonsoon period, there is a warming trend toward the north (Fig. 8f). A similar SST trend with northward propagation can be identified from the latitude–time plot of SST shown in Fig. 4d. A question is what processes control the temperature change from spring (premonsoon) to summer/winter. Seasonal temperature anomalies in the thermocline (Figs. 8d–f) may relate to cold/warm eddies (Figs. 7a,b). For example, during summer months, N1 was within a warm anticyclonic eddy (Fig. 7a) which coincided with the warm temperature anomaly (Fig. 8d), while N2–N5 were within cold eddies (Fig. 7a), that coincided with cold temperature anomalies (Fig. 8d). We suspect that part of these changes may attribute to heat transports by eddies and some of these aspects will be addressed in section 5. Standard deviations which basically represent intraseasonal variability, were largest in the thermocline near 100 m, especially at N5, where large isotherm displacements were observed during summer and winter (Fig. 3) associated with passages of large cyclonic and anticyclonic eddies (Fig. 7a).

5. Intraseasonal variability

a. Hovmöller diagrams of sea surface height anomalies

Time–longitude plots or Hovmöller diagrams of SSHA have been commonly used to examine the strength and propagation characteristics of seasonal to intraseasonal variability in the BoB (e.g., Girishkumar et al. 2011). In the following we adapt a similar approach to explore properties of SSHA-ISOs for the period of our moored observations. In general, SSHAs follow thermocline displacements, which in turn help to evaluate propagation characteristics of thermocline variability (Wunsch 1997). Figure 9 displays time–longitude plots of SSHA representing unfiltered (left panel), 60–90-day (middle panel), and 10–60-day (right panel) bands. The unfiltered SSHA shows westward-moving seasonal and subseasonal variability. As shown in Fig. 9, the 60–90-day SSHA-ISOs were weakest at N1, and N2, but more active near N5, while they were more common north of 10°N. However, most of the 60–90-day band oscillations were active after July 2019, i.e., after the recovery of our moorings, and also away from the moorings (Figs. 9e–h). The 10–60-day band was patchy in space and time, but activity appeared throughout the year with the strongest signal in winter. The low-frequency end of ISOs (60–90 day) propagated westward at a speed of 10–12 cm s^{-1} near 12°–14°N, while the high-frequency end of ISOs (10–60 day) propagated at speeds roughly 17–28 cm s^{-1} at 8°N, and 11–12 cm s^{-1} at 14°N.

b. Wavelet spectra

During MISO events, the atmospheric boundary layer and the upper ocean are coupled through multiple space–time-scale processes, and many of these processes are nonstationary, localized and contain sharp transitions. Here we adapted the wavelet transform, a nonstationary signal-processing technique (Morlet et al. 1982; Grossmann and Morlet 1984; Torrence and Compo 1998; Mallat 1989) to quantify strengths, temporal scales, and timings of ocean and atmosphere processes. We used Morlet wavelets to construct the wavelet spectra (sometimes referred to as scalograms), as a function time (t) and period (p_d) using commercially available MATLAB software. The wavelet spectrum for a given variable, X was computed by first obtaining a complex wavelet-transform series $\hat{X}$ by applying a continuous wavelet transform, and then the wavelet spectrum $\Psi_X(t, p_d)$ was computed (e.g., Torrence and Compo 1998). Figures 10–12 display wavelet spectra of zonal wind stress $[\Psi_{\tau x}(t, p_d)]$, wind stress curl $[\Psi_{\text{curl}}(t, p_d)]$, SSHA $[\Psi_h(t, p_d)]$, 26°C isotherm displacement $[\Psi_\eta(t, p_d)]$, zonal velocity $[\Psi_U(t, p_d, z)]$, and meridional velocity $[\Psi_V(t, p_d, z)]$ at depth $z = 120$ m at N1, N4, and N5 sites, respectively. Note that frequency is p_d^{-1}. Time scales of ISOs at N1 have similarities

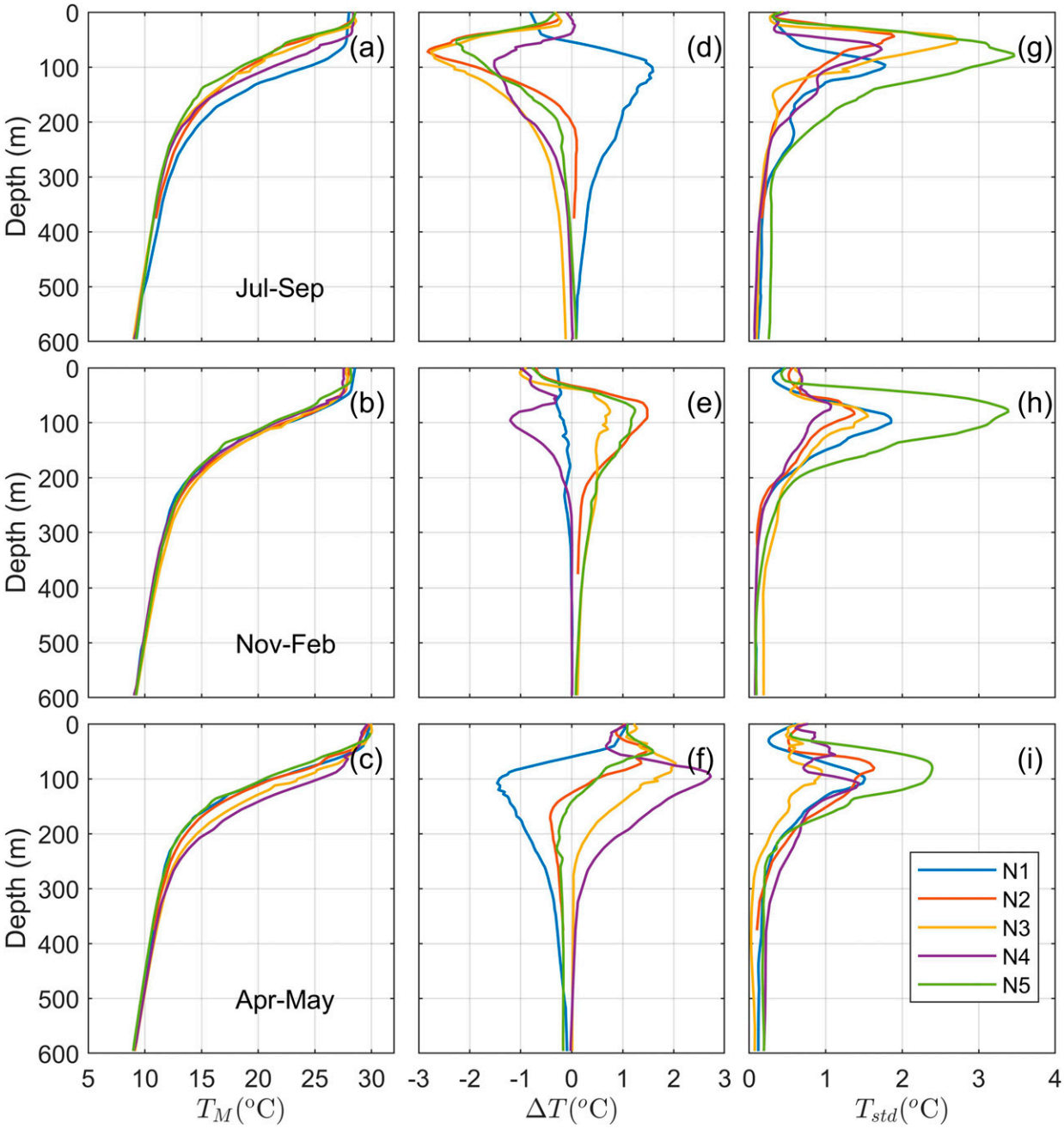

FIG. 8. Profiles of seasonal-mean temperature (T_M), temperature difference between seasonal mean and the annual mean (ΔT), and standard deviation (T_{std}) representing (a),(d),(g) summer monsoon (July–September), (b),(e),(h) winter monsoon (November–December), and (c),(f),(i) presummer monsoon (April–May).

with those at N2 and N3, and therefore wavelet spectral plots at N2 and N3 are not presented here. Wavelet spectra were computed for daily averaged ERA5 wind stress products and AVISO SSHA, and hourly averaged currents and temperature.

At N1, wavelet spectra of wind stress show a strong 30–40-day ISO band during June–August, followed by a weaker ISO band extending to the end of December 2018 (Fig. 10a). The 30-day ISO winds developed again after May 2019 as part of the monsoon annual cycle. Spectra of wind stress curl show similar oscillations during June–August 2018 (Fig. 10b). Furthermore, summer monsoon forcing contains pulses of high-wind stress and curl at higher-frequency bands. These short-duration wind events are separated by 2–6 weeks, and some isolated events are associated with severe storms, e.g., Cyclone Fani in April–May 2019. The 40–60-day SSHA-ISO

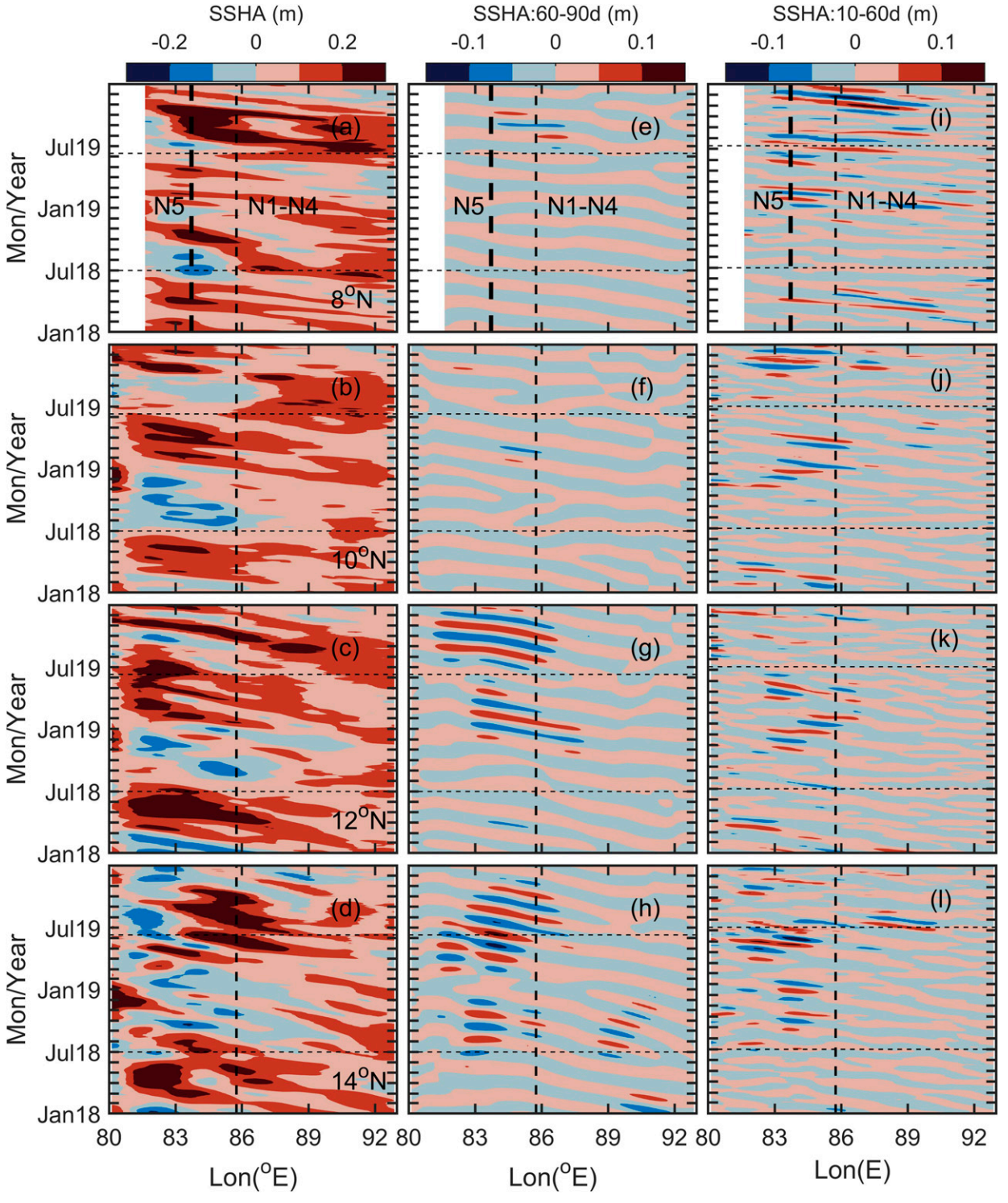

FIG. 9. Time–longitude plots (Hovmöller diagrams) of AVISO SSHA at mooring locations for (a),(e),(i) 8°, (b),(f),(j) 10°, (c),(g),(k) 12°, and (d),(h),(l) 14°N. Shown are (left) unfiltered SSHA, (center) 60–90-day bandpass-filtered SSHA, and (right) 10–60-day bandpass-filtered SSHA. The thin dashed and thick dashed vertical lines represent longitudinal position of N1–N4 and N5, respectively. Thin dashed horizontal lines are the start and end of mooring observations.

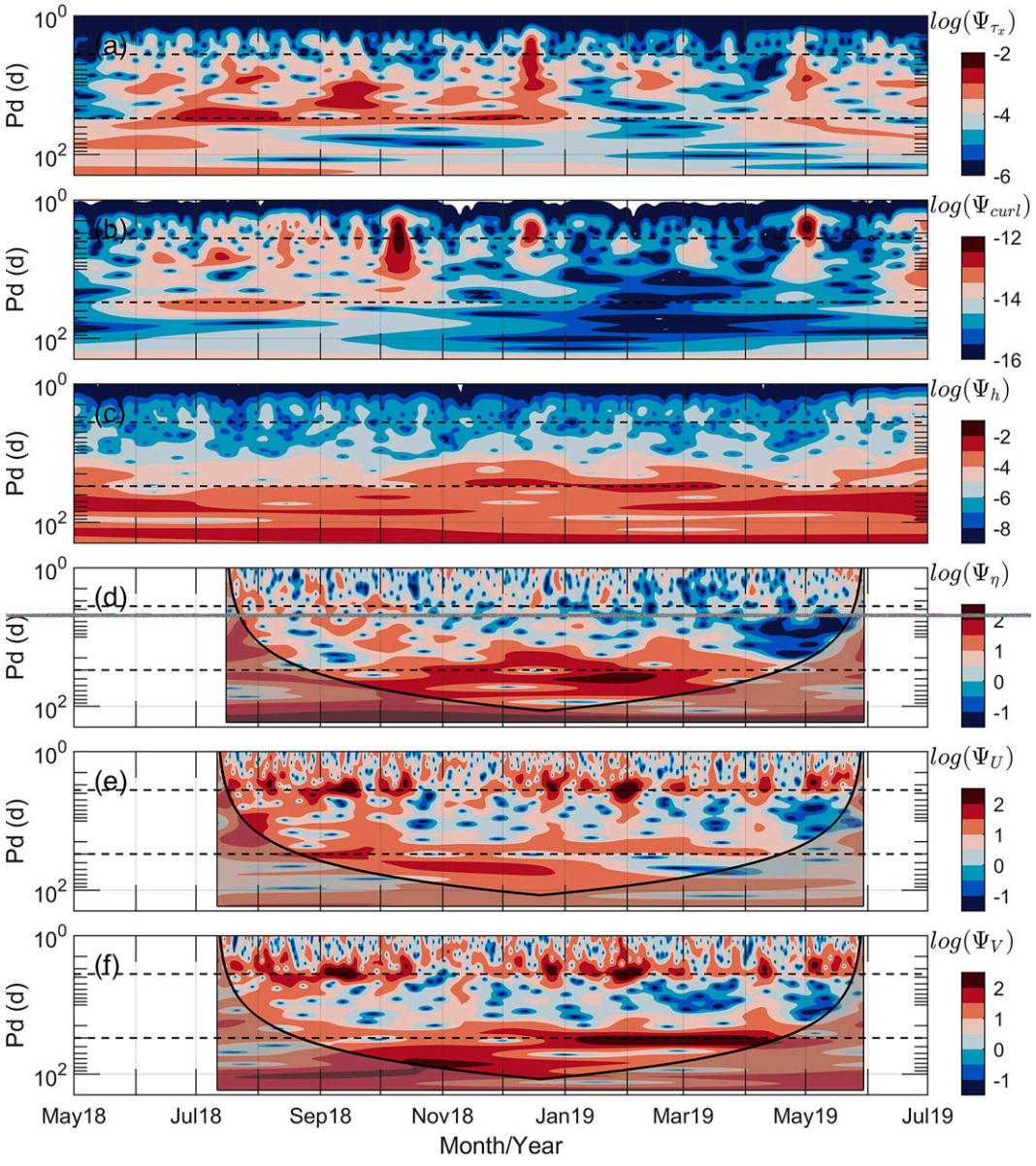

FIG. 10. Wavelet spectra at N1 plotted as a function of period (p_d) and time (t): (a) zonal wind stress $\Psi_{\tau x}(t, p_d)$ (N m^{-2})^2 and (b) wind stress curl $\Psi_{\text{curl}}(t, p_d)$ (N m^{-3})^2 from hourly ERA5, (c) SSH anomaly $\Psi_h(t, p_d)$ (m^2) from daily AVISO, (d) 26°C isotherm displacement $\Psi_\eta(t, p_d)$ (m^2) from hourly averaged moored thermistor measurements, (e) zonal velocity $\Psi_U(t, p_d)$, and (f) meridional velocity $\Psi_V(t, p_d)$ (m s^{-1})^2 at 120 m from hourly averaged ADCP currents. Thin dashed lines are inertial frequencies (top line) and 30-day periods (bottom line).

developed during most of the observational period, while a strong 20–30-day SSHA-ISO band, found between November and March, coincided with the 26°C isotherm variability (Figs. 10c,d). We noted similar wavelet spectra of 20°, 23°, and 26°C isotherms, and therefore, only the wavelet spectrum of the 26°C isotherm is presented here. Figures 10c and 10d further indicates that the 40–60-day temperature (or isotherm displacement) ISOs closely follow the SSHA-ISOs. Velocity spectra (Figs. 10e,f) show ~60-day oscillations throughout summer and winter, and then 30-day oscillations emerged starting in November with a strong meridional velocity component (Figs. 2 and 10f). During winter at N1, 30-day oscillations dominate SSHA and thermocline displacements, and currents. However, the timing of these oceanic ISOs is not directly correlated to the atmospheric winds, implying that the 30-day oceanic ISOs, found during winter, are not directly forced by 30-day wind stress curl associated with summer monsoon winds.

Wind speeds at N2–N4 are similar to winds at N1, but the strength of the wind stress curl at low frequencies (30-day

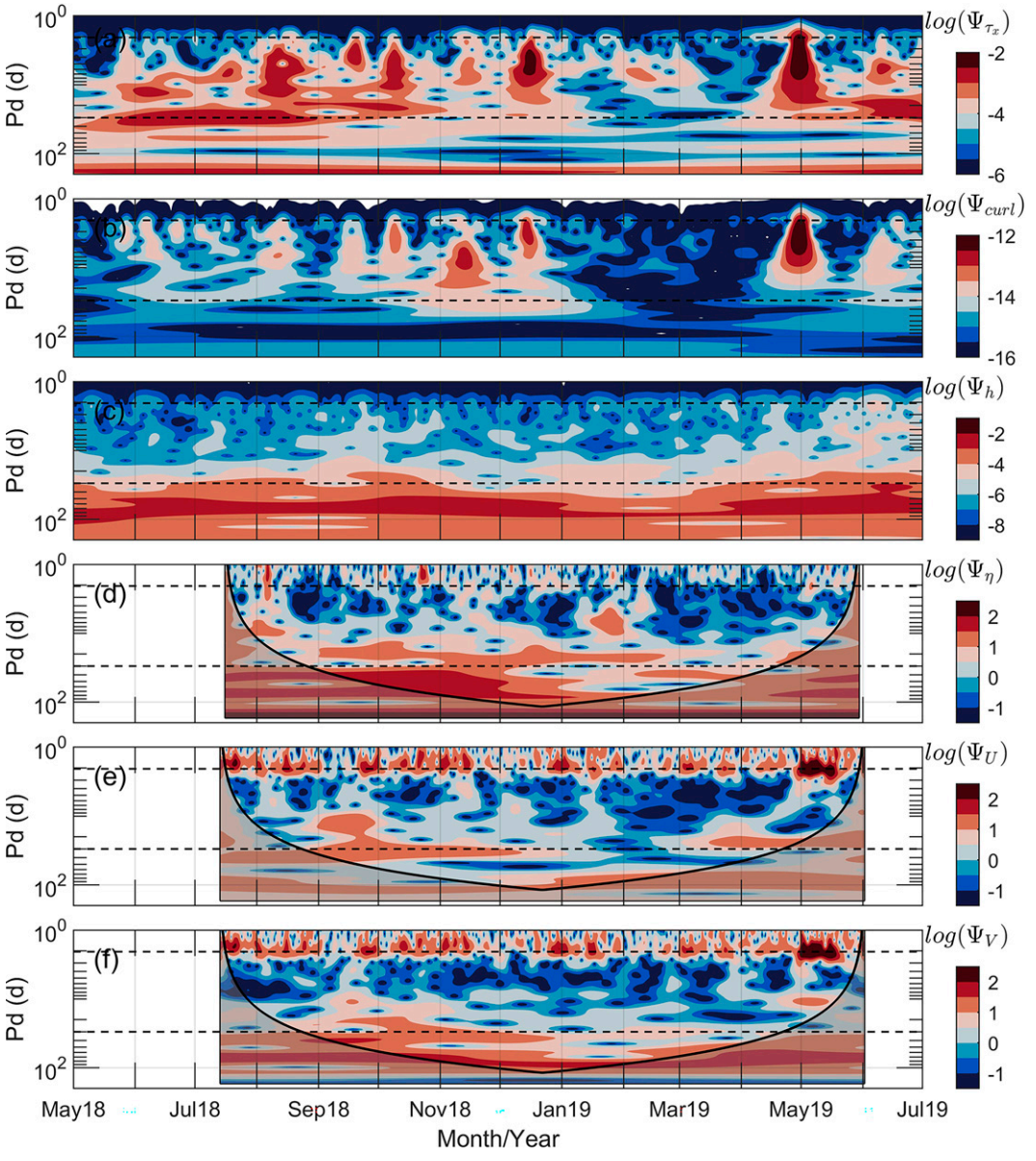

FIG. 11. As in Fig. 10, but for N4.

period to seasonal cycle) decreases toward the north (Figs. 4a–c). At N4, pulses of wind stress and curl dominated wind forcing, while high wind stress curl was associated with severe storms (Figs. 11a,b). At N4, the 30-day SSHA-ISO, isotherm displacement, and U and V variability disappeared during winter, which is a significant difference between N1 (Fig. 10) and N4 (Fig. 11).

N5 experienced the strongest local wind stress curl compared to the rest of the mooring sites (Figs. 10a,b, 11a,b, and 12a,b). At N5, the wind stress curl was large and positive, and was associated with time scales ranging from days to several months (Fig. 12b). The positive wind-stress curl (Fig. 4c) would likely generate a large negative SSHA (~−0.2 m) in June–September (Figs. 7a, 9a) through Ekman pumping. Note that N5 (8°N, 83.75°E) is about 120 n mi (≈222 km) from the east coast of Sri Lanka, where the SLD is typically formed.

c. Heat content

Heat content per unit area for a given depth is estimated as

$$\mathrm{HC}_d = \int_0^d \rho C_p T \, dz, \tag{1}$$

where ρ is the seawater density, C_p is the specific heat of seawater, and d is the depth of interest; d can be either the depth of 26°C isotherm, or a fixed layer depth, say 200 m, or the mixed layer depth. The mixed layer depth represents the

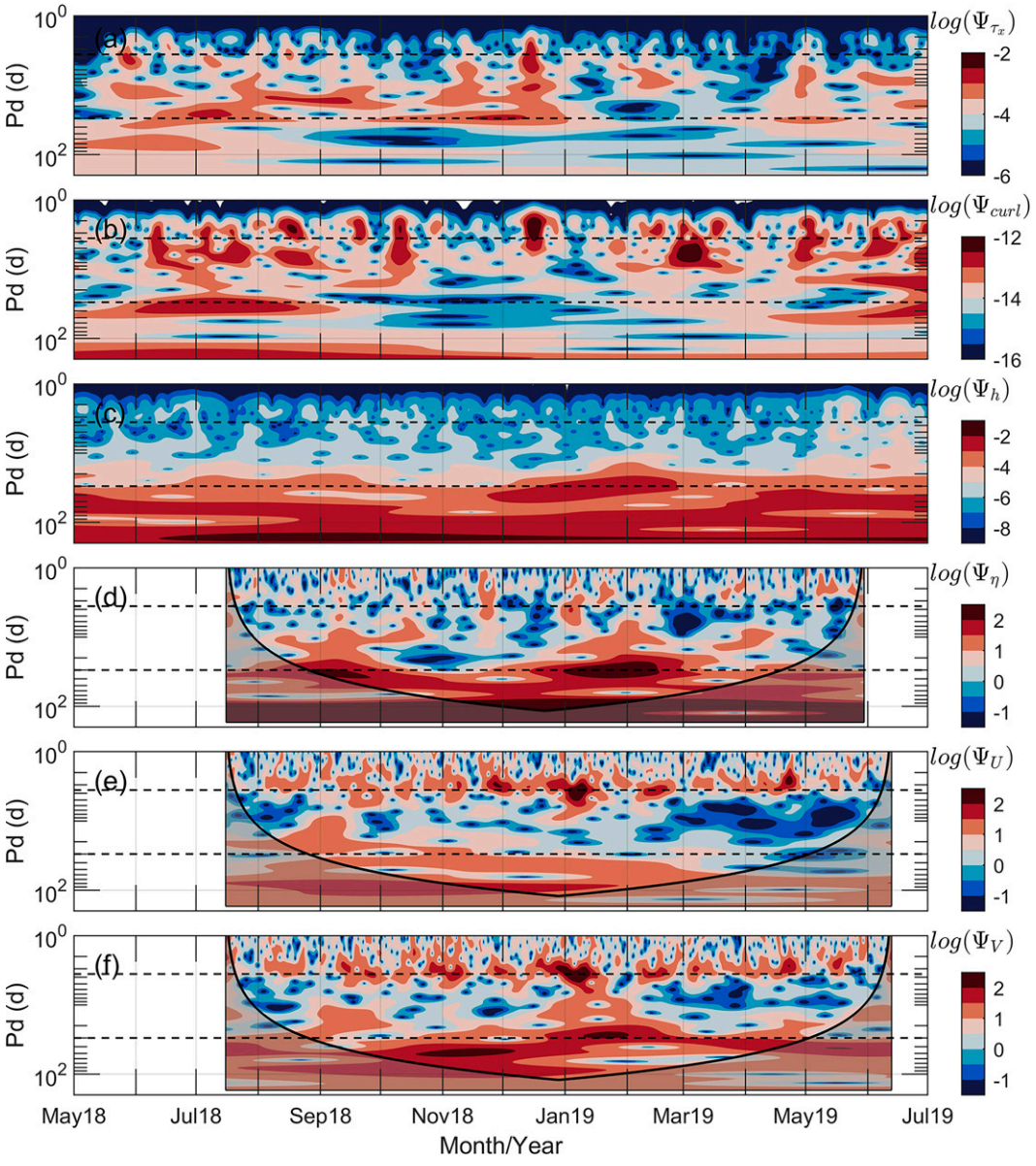

FIG. 12. As in Fig. 10, but for N5.

penetration depth of local surface buoyancy and wind stress forcing through turbulent mixing processes, but the determination of the mixed layer depth is not a trivial task due to lack of salinity observations in the upper 100 m. Therefore in our analysis, d represents either the depth of the 26°C isotherm or 200 m. The 26°C isotherm is also an attractive choice since the tropical cyclone heat potential is defined as the total heat content above the 26°C isotherm (Leipper and Volgenau 1972; Jaimes et al. 2016). Near-surface temperatures have gaps due to failures and losses of thermistors on mooring lines. These temperature gaps were filled by interpolating temperature profiles between the shallowest moored measurement and the temperature at the surface (i.e., daily-averaged satellite SST). We noted (not shown here), based on CTD profiles taken along the mooring array during the deployment (July 2018) and the recovery (June 2019) of moorings, that a weakly stratified layer above the thermocline was at depths of about 20–40 m. Therefore, the linear interpolation may not generate significant errors in the estimates of heat content for low frequencies (periods $>$ 10 days). Figure 13 shows 10-day low-passed heat content at five mooring sites above the 26°C isotherm (Figs. 13a,b), and 200-m depth (Figs. 13c,d). Both estimates show 20–60-day intraseasonal variability at N1–N4, but at N5, lower-frequency variability dominated during summer and fall. A warm anticyclonic eddy with high heat content passed N1 in August–September (Figs. 7a, 9a), and nearly a month later, it passed through N5, suggesting that the eddy moved westward at a speed of about 9 cm s^{-1}. Prior to the

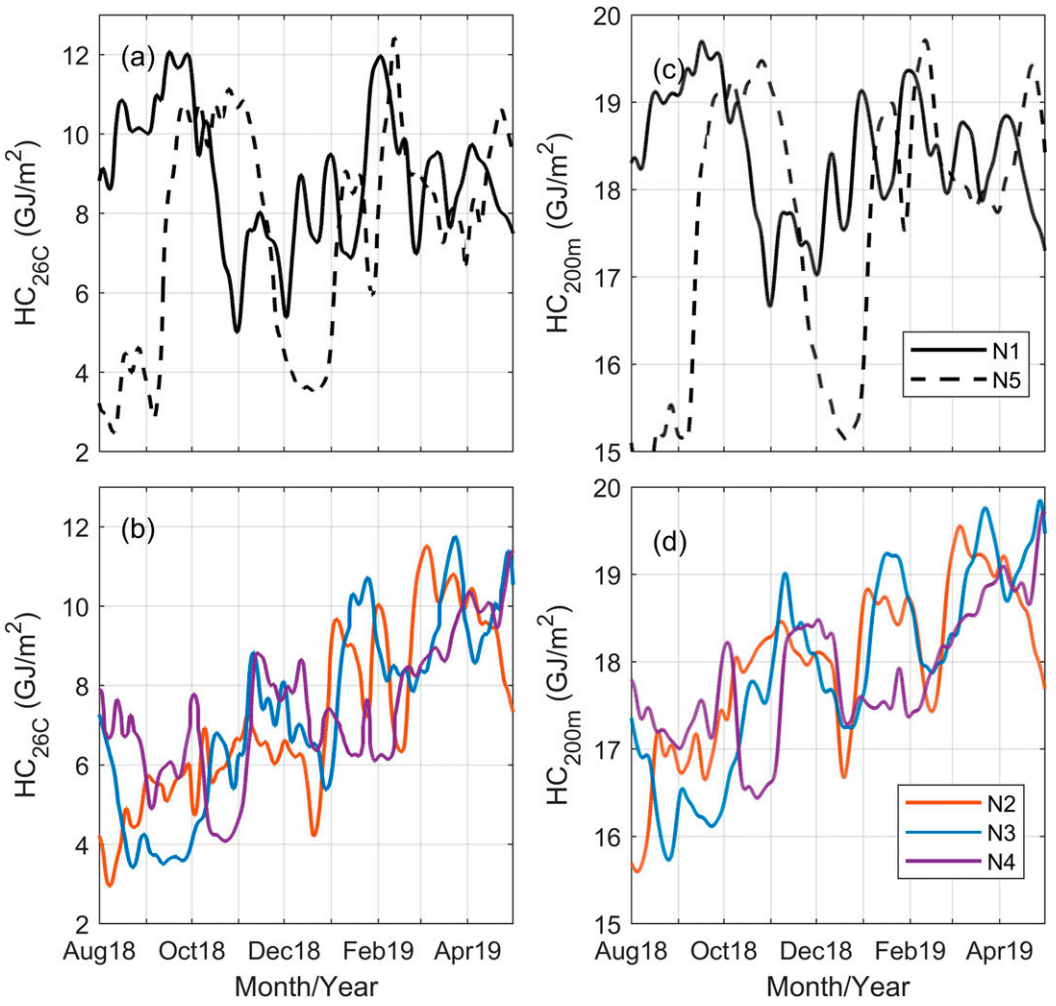

FIG. 13. Heat content (left) above the 26°C isotherm and (right) above 200 m. (a),(c) Heat content at N1 and N5 and (b),(d) heat content at N2, N3, and N4.

arrival of an anticyclonic eddy at N5, a cyclonic eddy (SLD) passed the same location in July–August (Figs. 7a, 9a, and 13a,c), thus generating large fluctuations in heat content. For example, during the transition from the cold cyclonic eddy to the warm anticyclonic eddy in August 2018, the heat content above the 26°C isotherm at N5 changed from 3 to 11 GJ m^{-2} or nearly by a factor of 4 change (Fig. 13a). N1 registered 20–30-day oscillations after the passage of these large eddies in November, while N2 and N3 registered close to 30–60-day oscillations throughout observational period. At N1–N3, the changes in heat content for 20–60-day ISOs were about 2–4 GJ m^{-2}, which is smaller than that of seasonally varying eddies observed at N5 (Figs. 9a, 12). N4 registered weak intraseasonal variability.

6. Heat fluxes

a. Flux estimates from wavelet cospectral method

The wavelet spectra of isotherm displacements and velocities reveal multi-time-scale ISOs with considerable nonstationarity in space (i.e., mooring sites) and time (Figs. 10d–f, 11d–f, and 12d–f). These ISO bands may carry heat and salt within and also in and out of the BoB. In the following we examine the spectral properties of heat-flux-carrying ISO bands using a continuous wavelet transform techniques (e.g., Torrence and Compo 1998). Recently, wavelet cospectral methods have been applied successfully to estimate atmospheric boundary layer heat and momentum fluxes (Laxague et al. 2018). In the following, temperature fluxes for selected frequency bands at a given depth are computed from cowavelet spectra (sometimes referred as coscalograms) as a function of time and period, where the corresponding frequency is the inverse of the period. As discussed before, a continuous wavelet transform analysis (Torrence and Compo 1998; Mallat 1989) was applied to velocity $[U(t, z), V(t, z)]$ and temperature $[T(t, z)]$ time series, yielding complex transform series for velocity $[\hat{U}(t, p_d, z), \hat{V}(t, p_d, z)]$ and temperature $[\hat{T}(t, p_d, z)]$, and then cowavelet spectra of zonal, and meridional heat fluxes, $\Psi_{UT}(t, p_d, z)$, and $\Psi_{VT}(t, p_d, z)$, were estimated as a function of time, where

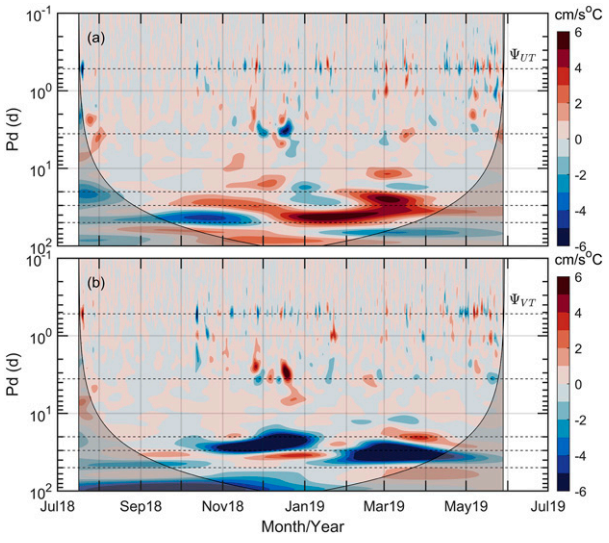

FIG. 14. (a) Wavelet cospectrum of zonal heat flux $\Psi_{UT}(t, p_d)$ and (b) meridional heat flux $\Psi_{VT}(t, p_d)$ as function of period and time at N1, at 64-m depth. Horizontal black dashed lines are at 0.52- (semidiurnal), 3.58- (inertial), 20-, 30-, and 50-day periods. Transparent-gray shading indicates truncation due to cone of influence limits.

$$\Psi_{UT}(t, p_d, z) = \mathrm{Re}(\hat{U}\hat{T}^*), \tag{2}$$

$$\Psi_{VT}(t, p_d, z) = \mathrm{Re}(\hat{V}\hat{T}^*), \tag{3}$$

and "Re" and an asterisk (*) denote the real part and the complex conjugate, respectively. Cowavelet spectra of heat fluxes were computed for all the mooring sites at multiple depths using 318-day-long times of velocity and temperature, and short records of velocity were not used in wavelet heat-flux estimates.

Figure 14 shows an example of Ψ_{UT} and Ψ_{VT}, plotted as functions of time and period at mooring N1 at 64 m. The fluxes are in cm s^{-1} °C. The green shading in the plots indicate the cone of influence truncation from the wavelet analysis. Persistent but intermittent flux is apparent in the semidiurnal band, and there was an event in December 2018, in the inertial band, which may be related to the Tropical Cyclone Phethai (http://rsmcnewdelhi.imd.gov.in/uploads/report/26/26_963896_phethai.pdf). The predominant fluxes were roughly between periods of 10 and 40 days, and were directed primarily southeastward with maximum values exceeding 6 cm s^{-1} °C at this depth. Longer periods were likely also important, but record length limitations, preclude accurate results for these scales. Wavelet fluxes at moorings N2 and N3 at 120 m show fluxes at 30-, 40-, 50-, and 60-day periods, but wavelet cospectra partially resolve fluxes at periods larger than 40 days.

The Ψ_{UT} and Ψ_{VT}, as functions of depth and time, for periods of 10, 20, 30, and 40 days have been examined, and 25–35-day band-averaged fluxes are plotted in Fig. 15 for moorings N1–N5. Records at shallower depths than about 120 m at N2, N3, and N5, were shorter than the approximately 318 days of the deployment (see instrumentation section); hence, the minimum depths in Fig. 15 vary, and the plots are limited to full-length records. However, for the 10-day case where shorter records could be used (not shown here), temperature fluxes were intermittent, mostly eastward and northward at shallower depths. In December–April, a several-month-long southward flux, with a magnitude exceeding 1.5 cm s^{-1} °C at N1 occurred above 200 m. Significant flux magnitudes extended deeper for the longer periods (not shown). The meridional fluxes at N1 were mostly southward over the entire period of the data, and a southeastward flux at N2 occurred above 200 m over much of the record. An eastward flux event was present at N4 in fall. At N5, a mostly southward flux occurred in October between 100 and 300 m. Eastward flux above 200 m at N5 was present in winter.

Mean profiles of heat flux, calculated for the 25–35-day band, show that most of the fluxes were limited to the upper 150 m. On average, fluxes at N1–N3 were southwestward and the largest mean flux of about 2 cm s^{-1} °C occurred at N1 near 70 m; at N4 the mean fluxes were mostly eastward and confined to the upper 80 m with a maximum flux of about 2 cm s^{-1} °C at 30 m. The errors about the means of the observed average-flux profiles for 25–35-day periods are about 0.25 cm s^{-1} °C or less near the tops of the mean profiles, and gradually decrease to about 0.1 cm s^{-1} °C or less at depths of about 150 m and deeper.

b. 10–60-day ISO fluxes from covariance method

As discussed above, the wavelet cospectral technique shows that heat is transported by multiple time-scale motions, including 10-, 20-, and 25–35-day ISOs. While the wavelet method clearly helps to identify multiple ISOs and timing of their occurrences, the wavelet spectra can represent only a fraction of ISO bands for periods greater than 40 days due to the relatively short record length of our observations. We noted, however, that 10–60-day ISOs dominate in velocity, temperature, and heat content (Figs. 2, 10–13) and SSHA (Fig. 9). Therefore, in the following, eddy heat fluxes, $\langle U'T' \rangle$ and $\langle V'T' \rangle$ for the 10–60-day ISOs were computed from the covariance of temperature and velocity components, where the prime denotes the 10–60-day band, and angle brackets denote the averaging time scale or record length for the estimated flux. For a given depth, $\langle U'T' \rangle$ and $\langle V'T' \rangle$ were estimated by computing covariance of U' and T', and V' and T' for every 60-day record, respectively. We estimated fluxes using overlapping 60-day records to produce smooth flux estimates with time. Heat fluxes were computed for all five mooring sites, and a detailed example is given in Fig. 16. Figure 16 displays 10–60-day ISO velocities, temperature, and eddy fluxes along with eddy kinetic energy. ISO velocities and KE were measured as deep as 600 m, but they were strongest in the upper 250 m with velocity fluctuations as large as ±30 cm^{-1} in the upper 75 m. During October 2018, a subsurface-intensified eddy-like feature passed the N1 site having large

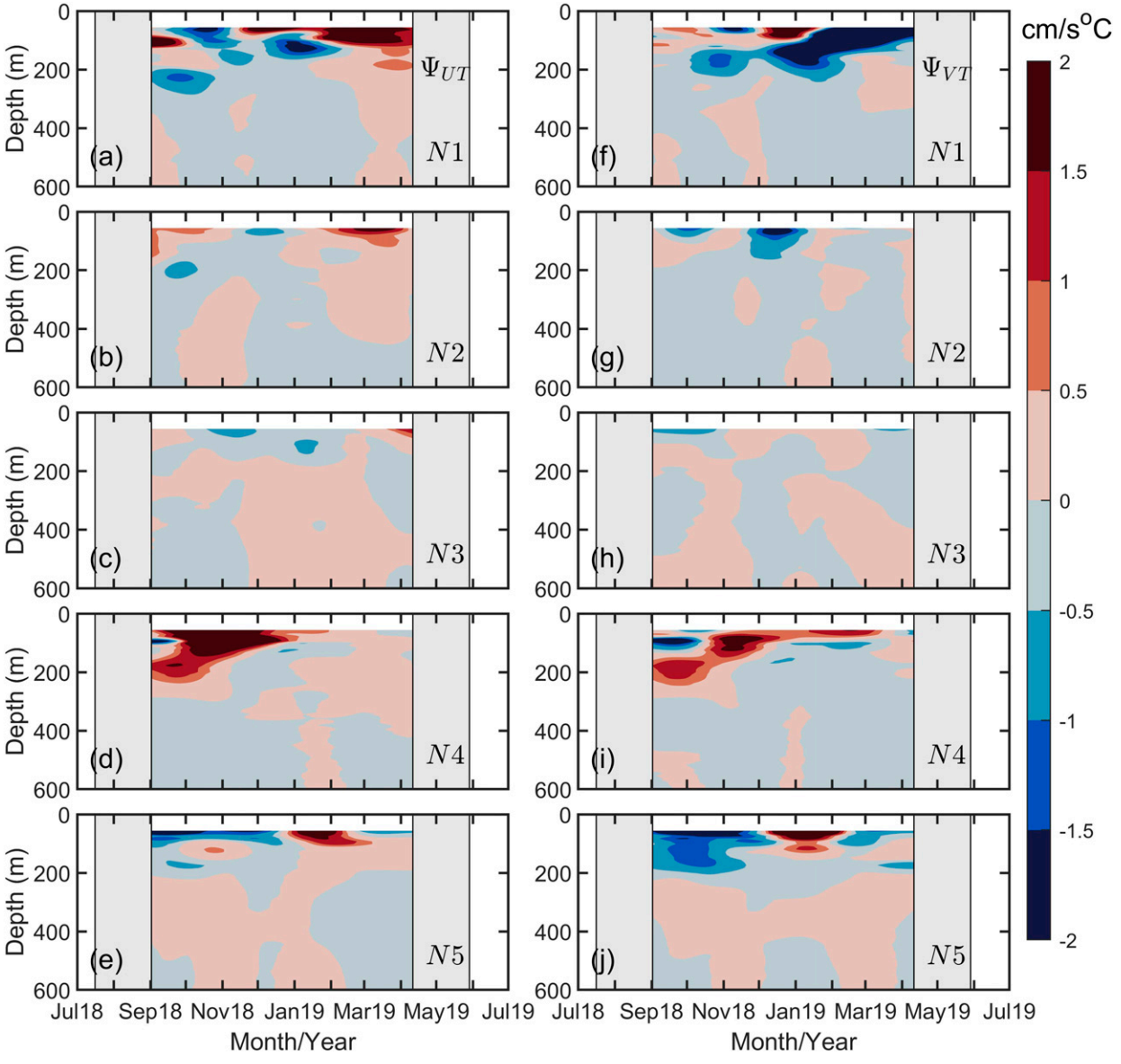

FIG. 15. The 25–35-day band-averaged wavelet cospectrum of (left) zonal heat flux $\Psi_{UT}(t, z)$ and (right) meridional heat flux $\Psi_{VT}(t, z)$ for moorings N1–N5 as function of depth and time. Gray shading indicates truncation due to cone of influence limits.

velocity and temperature fluctuations, and a similar feature was observed at N4. Temperature ISOs were as large as ±3°C in the thermocline near 100-m depth, and eddy heat fluxes as large as ±6 cm s^{-1} °C occurred in the thermocline near 50–100-m depths. Below the thermocline fluxes decayed rapidly with depth. The direction of $\langle U'T' \rangle$ changes with time and depth, while $\langle V'T' \rangle$ is negative or southward. Similar flux patterns were found at N2–N4, but $\langle V'T' \rangle$ at N4 was small compared to that at N1. Heat fluxes at N5 were large mainly due to contamination of seasonally varying eddies such as the SLD.

To examine vertical structure of $\langle U'T' \rangle$ and $\langle V'T' \rangle$ at the five mooring sites, we computed time-averaged vertical profiles. Time-averaged $\langle U'T' \rangle$ and $\langle V'T' \rangle$ profiles (Fig. 17) show that both zonal and meridional fluxes are limited to the upper 250 m, and strongest in the thermocline near 75 m. In general $\langle V'T' \rangle$ is negative or southward along the moorings, except at N5 (Fig. 17b), where seasonally varying eddies are stronger. On average, $\langle U'T' \rangle$ is positive or eastward, but relatively small compared to $\langle V'T' \rangle$, except at N5 (Fig. 17a). To further examine meridional variability of fluxes, heat fluxes were averaged into two layers, where the upper layer carries maximum transports between 40 and 96 m, which lies below the mixed layer and above the top of the strongly stratified thermocline, and the lower layer is between 96 and 200 m. Time- and layer-averaged fluxes (Table 2) in the upper layer reveal $\overline{\langle V'T' \rangle}$ is about 2.2 cm s^{-1} °C at N1–N3, and is about −0.44 cm s^{-1} °C at N4, indicating a strong meridional heat-flux

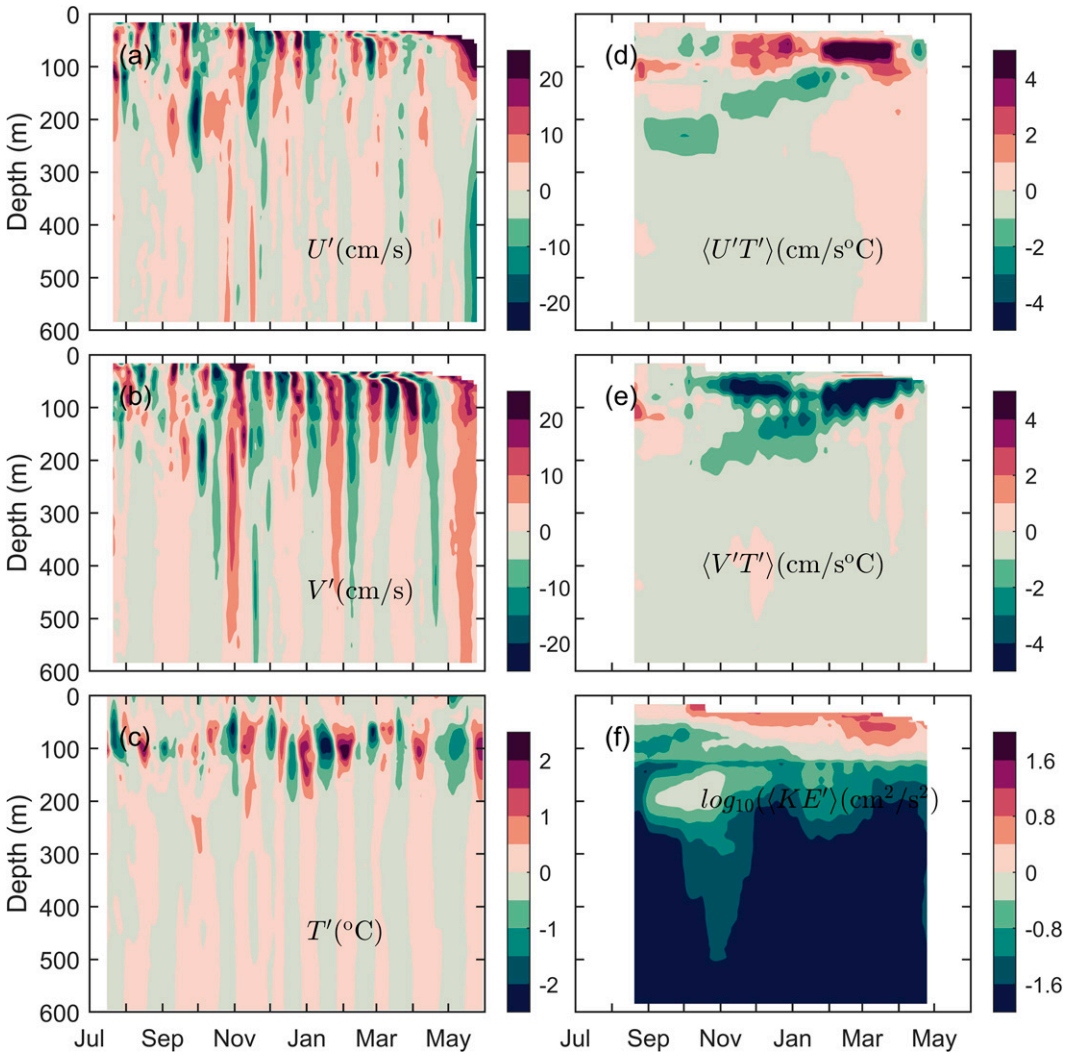

FIG. 16. The 10–60-day bandpass-filtered (a) zonal velocity U', (b) meridional velocity V', (c) temperature T', (d) estimated zonal heat flux $\langle U'T'\rangle$, (e) meridional heat flux $\langle V'T'\rangle$, and (f) eddy kinetic energy (KE′) at N1. The angle brackets denote the length of the record (i.e., 60 days) used in the flux calculation.

divergence between 12° and 14°N. In general, fluxes are small in the lower layer between 96 and 200 m. Standard error bars in Table 2 were based on the total number independent samples in each layer. We will discuss the flux divergences in the discussion.

7. Discussion

a. Local forcing versus remote forcing

The oceanic ISOs in the BoB can be formed either by the remote forcing originating from the eastern boundary through Kelvin/Rossby wave propagations or by the local wind forcing through Ekman pumping, or by the combination of both. Willebrand et al. (1980) examined analytical and numerical solutions of oceanic response to large-scale atmospheric disturbances. They noted three distinct frequency bands to describe the wind-driven barotropic fluctuations, which include 1) waves with periods from inertial to a week, 2) planetary Rossby waves with periods from a week to a month, and 3) time-independent currents with Sverdrup balance. As discussed in sections 3 and 4, wind forcing (wind stress and curl) comprises synoptic time scales, 25–35 days, and seasonal variability, while the curl was strongest in the southern BoB (Figs. 4c, 10b–12b). It is likely that the synoptic-time-scale wind forcing can generate near-inertial waves as observed in moored velocity records (Figs. 10–12). The 30-day ISOs of surface wind stress curl (Figs. 10a,b, 11a,b, and 12a,b) and oceanic currents (Figs. 10e,f, 11e,f, and 12e,f) were observed at several mooring sites. The wind stress curl ISOs at 30-day periods occurred during July–August, whereas the corresponding oceanic (velocity and isotherm displacements) ISOs occurred in November–February, indicating that the time lag between atmospheric and oceanic

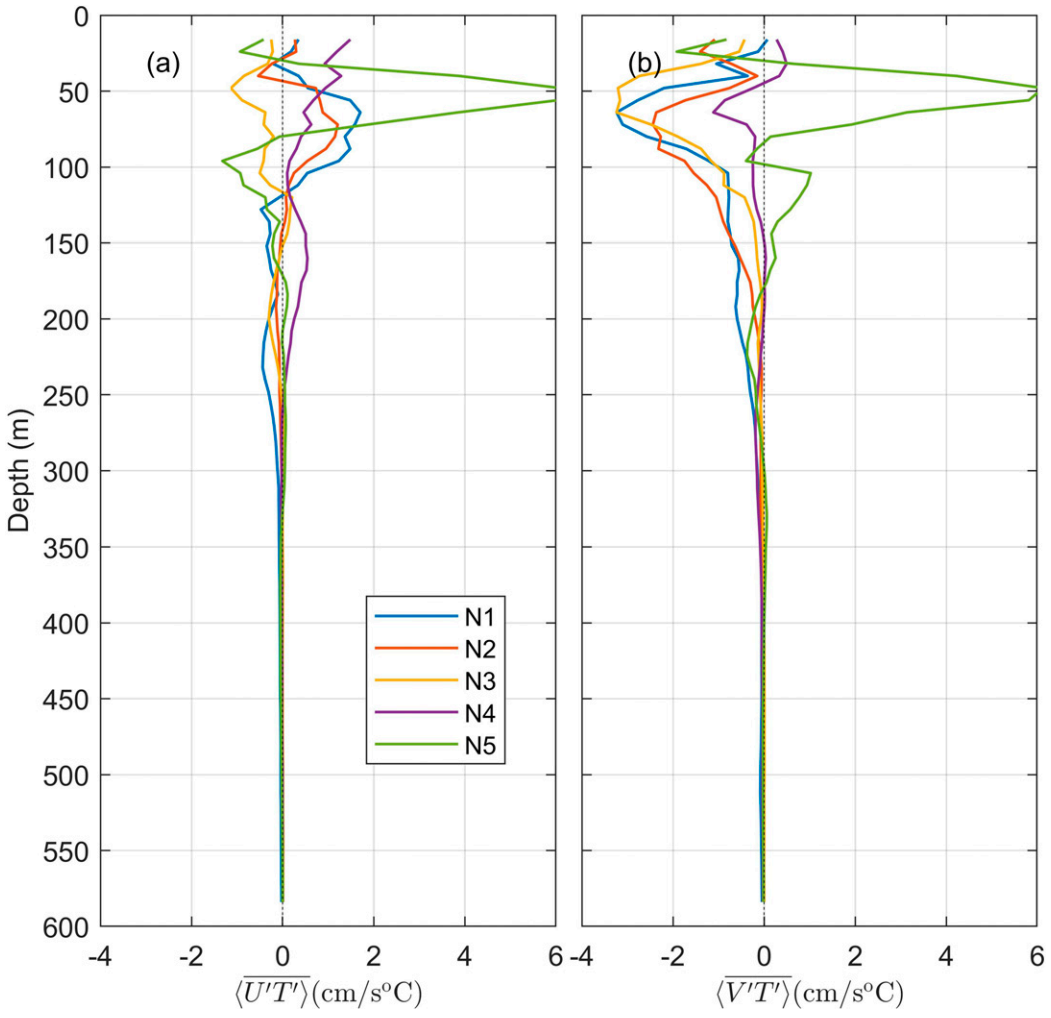

FIG. 17. Time-averaged heat-flux profiles (a) zonal and (b) meridional components.

ISOs is larger than 3 months. Therefore, it is unlikely that direct wind forcing would generate the observed oceanic ISOs with 30-day periods. These oceanic ISOs propagate westward and are most likely controlled by the remote forcing at the eastern boundary. However, near N5, the SLD formed during June–September. The SLD is suggested to be formed by the seasonal wind stress curl, and therefore strong wind-driven upwelling can be expected (e.g., Cullen and Shroyer 2019). The Ekman pumping velocity W_E was computed from ERA5 winds while considering both wind stress

TABLE 2. 10–60-day ISO heat fluxes at mooring sites. Fluxes are averaged for two selected depth ranges and time for the mooring deployment period of 11 months, where $\langle\overline{U'T'}\rangle$ is the zonal heat-flux component, and $\langle\overline{V'T'}\rangle$ is the meridional heat-flux component. Averaging-depth ranges are 40–96 m and 96–200 m (where heat fluxes are largest; Fig. 17). The data coverage in the upper 40 m is sparse due to gaps in velocity and temperature, and therefore we exclude them.

	40–96 m		96–200 m	
Location	$\langle\overline{U'T'}\rangle$ ± std error (cm s^{-1} °C)	$\langle\overline{V'T'}\rangle$ ± std error (cm s^{-1} °C)	$\langle\overline{U'T'}\rangle$ ± std error (cm s^{-1} °C)	$\langle\overline{V'T'}\rangle$ ± std error (cm s^{-1} °C)
N1	1.24 ± 0.27	−2.20 ± 0.32	−0.15 ± 0.11	−0.68 ± 0.12
N2	0.59 ± 0.17	−1.50 ± 0.16	−0.04 ± 0.06	−0.69 ± 0.07
N3	−0.54 ± 0.21	−2.20 ± 0.17	−0.06 ± 0.07	−0.22 ± 0.04
N4	0.46 ± 0.25	−0.44 ± 0.22	+0.35 ± 0.08	−0.07 ± 0.06
N5	1.06 ± 0.30	+2.40 ± 1.08	−0.22 ± 0.10	+0.30 ± 0.24

curl and beta effect, given by $W_E = \nabla \times \boldsymbol{\tau}/(pf) + \beta\tau_x/(pf^2)$, where ρ is the density of seawater, f is the inertial frequency, and $\beta = 2.3 \times 10^{-11}$ m^{-1}s^{-1}. At N5, W_E shows 30-day oscillations similar to $\nabla \times \boldsymbol{\tau}$, τ_x, and τ_y during June–September (Figs. 4a–c, 12a,b) indicating that both seasonal and subseasonal winds control upwelling within the SLD. On average W_E is about 0.5 m day^{-1} with a maximum close to 1 m day^{-1} over the SLD (near N5; Fig. 7a), and similar magnitudes of vertical velocities were estimated near 8°N, 85.5°E during the summer of 2014 (Wijesekera et al. 2016).

b. Meridional heat-flux divergence

The transport of heat by ISOs occurred at multiple time scales as observed in cowavelet spectra (Fig. 14), and the eddy covariance method (Fig. 16) shows that the 10–60-day band contained significant heat fluxes. Here we examine meridional heat-flux divergences associated with the 10–60-day ISO band. The strongest $\overline{\langle U'T'\rangle}$ and $\overline{\langle V'T'\rangle}$ are observed at depths between 40 and 96 m (Table 2), where the meridional divergence of $\overline{\langle V'T'\rangle}$ is largest between N3 and N4, while $\overline{\langle V'T'\rangle}$ at N1, N2, and N3 are comparable. $\overline{\langle U'T'\rangle}$ is about one-third to half of $\overline{\langle V'T'\rangle}$, and eastward except at N3. The southward fluxes at N3 and N4 are about 2.2 and 0.44 cm^{-1} °C (Table 2), and the resulting average $\partial\overline{\langle V'T'\rangle}/\partial y$ in the upper layer for the 11-month observational period is about $+8.3 \times 10^{-8}$ °C s^{-1} (10.1×10^{-8}–6.4×10^{-8} °C s^{-1}), where values in parentheses are the expected maximum and minimum fluxes based on standard-error estimates. Even though the magnitudes of $\overline{\langle V'T'\rangle}$ are small in the lower layer, a gradual increase in southward heat transport clearly shows divergence of meridional heat flux between 10° and 14°N, where the southward fluxes at 10° and 14°N were about 0.70 and 0.07 cm s^{-1} °C, respectively (Table 2), and $\partial\overline{\langle V'T'\rangle}/\partial y$ in the lower layer is about $+1.4 \times 10^{-8}$ °C s^{-1} (1.7×10^{-8}–1.1×10^{-8} °C s^{-1}).

It is not a trivial task to evaluate the heat balance in the upper ocean along the mooring array, since many terms (advective and diffusive fluxes) in the heat balance equation are not available. Therefore the role of the heat transport by ISOs is evaluated by comparing, vertically integrated meridional heat-flux divergence, $\int_0^H \rho C_p \partial\overline{\langle V'T'\rangle}/\partial y\, dz$, and the net surface heating in the north-central bay (Qnet), where H is a depth at which flux gradients are negligible. The estimated $\int_0^H \rho C_p \partial\overline{\langle V'T'\rangle}/\partial y\, dz$, for H = 200 m is 20–30 W m^{-2}, where most of the contribution comes from the 40–96-m depth range (Table 2, Fig. 17). The heat transport by ISOs is comparable to the averaged ERA5-Qnet (~27 W m^{-2}) for the period between June 2018 and June 2019 at 8°–14°N, 86°E and is also same order of the annual average of measured Qnet (37 W m^{-2}) at the WHOI mooring (18°N, 89.5°E) (see section 4). Therefore, one can argue, that on an annual time scale, ISOs transport surface heat flux southward. However, the eddy transport in the upper 40 m is small (Fig. 17), and therefore vertical processes such as vertical mixing, submesoscale vertical fluxes, and wind-driven upwelling/downwelling in the northern bay must play a role by transporting surface heat flux into the thermocline.

The positive meridional flux divergence aids cooling in the thermocline, since $\partial\overline{T}/\partial t \sim \partial\overline{\langle V'T'\rangle}/\partial y$. The cooling in the thermocline (40–96 m; Table 2) on an annual time scale is about 2.6°C (2.1°–3.5°C). As noted in section 4c, the amount of cooling in the thermocline is a similar order of magnitude as the temperature drop in the upper 100 m (Figs. 8a–f) and SST (Fig. 4d) from late spring (April–May) to winter (December–February). Similar cooling effects in the thermocline were reported during May–October 2014 (Pirro et al. 2020a). Pirro et al. (2020a) also found that during the passage of ISOs, the thermocline cooled at a rate of about -10^{-7} °C s^{-1}, which can generate cooling of about 0.5°C for a period of 60 days.

c. Air–sea coupling: Oceanic heat content, SST, and OLR, and oceanic ISOs

It has been reported that the net surface heat flux associated with northward moving MISO-convective bands generate positive/negative SST fluctuations over the ocean (Sengupta et al. 2001) and oceanic heat content over the upper 40 m (Krishnamurti et al. 2017), where the time rate of change in SST can be proportional to the net surface heat flux (Sengupta and Ravichandran 2001).The oceanic ISOs such as eddies and planetary waves have comparable time scales to the active-break cycle of MISO events, and they generate thermal anomalies extending deep into the thermocline. Therefore, the intraseasonal variability of the upper-ocean heat content, found during the summer monsoon (Fig. 13), include both MISO-induced temperature anomalies and oceanic ISOs.

To explore plausible correlations between SST and OLR, and HC_{26} (heat content above the 26°C isotherm) and OLR, we use a wavelet coherence analysis to measure the short-lived localized coherences in time and frequency space for these two temporal measurements (e.g., Torrence and Compo 1998; Grinsted et al. 2004). Here, the wavelet coherence squared and the associated phase angle are computed for all the mooring sites using a MATLAB-based software (https://github.com/grinsted/wavelet-coherence; Grinsted 2021). We found significant wavelet coherences at multiple periods including 2–7-day synoptic variability to 10–60-day ISOs. In the following we describe coherences and phase relations of SST–OLR and HC_{26}–OLR at N1 and N4 mooring sites.

Figures 18 and 19 illustrate time series of SSHA (panel a), HC_{26}, SST and OLR (panel b), and squared wavelet coherences and relative phases of HC_{26}–OLR (panel c), and SST–OLR (panel d) at N4 and N1, respectively. The phase information is marked in arrows similar to the method suggested by Grinsted (2021), where the eastward arrows indicate no phase difference between SST or HC_{26} and OLR, westward arrows indicate 180° phase (or antiphase) differences, and downward arrows indicate 90° phase difference where SST and HC_{26} leads OLR.

Higher coherences (i.e., squared coherence > 0.5) occurred at synoptic scales to 10–60-day ISO bands (Figs. 18c, 19c). In general coherences at synoptic time scales are spotty or short

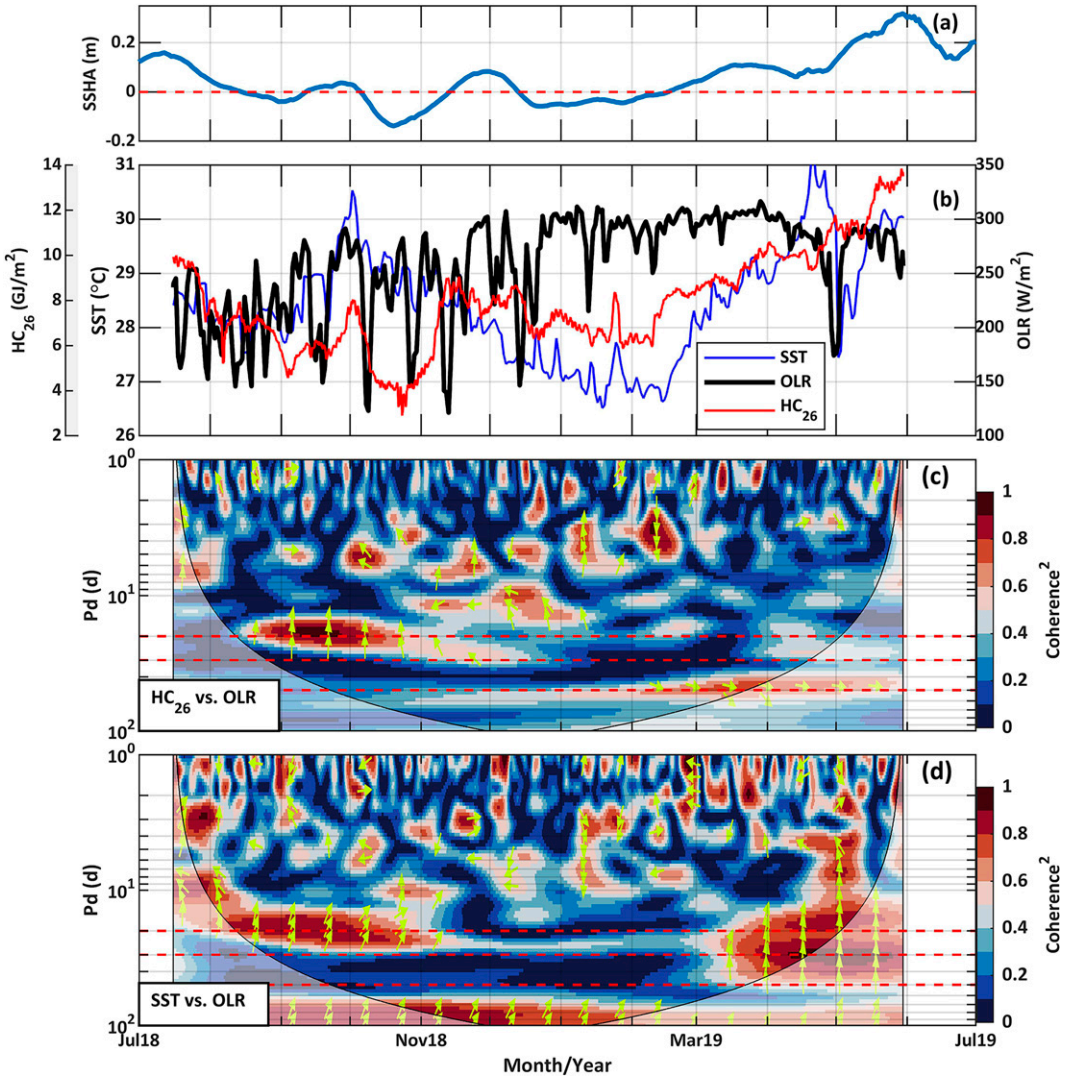

FIG. 18. (a) Time series of SSHA (thick blue line) at N4, and (b) heat content above the 26°C isotherm (HC_{26C}) (red line), SST (blue line), and OLR (thick black line). The squared wavelet coherence between (c) heat content and OLR and (d) SST and OLR are plotted as a function of time and period. Arrows indicate the relative phase between HC_{26} and OLR and between SST and OLR with in-phase pointing right, antiphase pointing left, HC_{26} or SST leading OLR by 90° pointing straight down, and HC_{26} or SST lagging OLR by 90° pointing straight up. The red dashed lines are at 20-, 30-, and 50-day periods.

lived. We noted lag and lead coherences between SST/HC_{26} and OLR, including large coherences during severe storms. For example, high coherences between SST and OLR for periods of 5–50 days in late April–early May (Fig. 18d) are associated with Cyclone Fani (Figs. 4a,b and 5). Here SST lagged OLR by approximately 90° for the 5–50-day band, or SST lagged OLR by 1–12 days, which is consistent with the formation of a cold wake along the path of the cyclone (Fig. 4d). However, such large coherences were not found between HC_{26} and OLR (Fig. 18c). As shown in Fig. 18b, both SST and HC_{26} increased steadily during April–May 2019, and then SST and OLR dropped significantly during the passage of Fani. But the drop in HC_{26} was small, partly because, the 26°C isotherm was as deep as 100 m (Fig. 3f) and associated with warm eddy (Fig. 18a). We note that at the N3 mooring site, both SST and HC_{26} lagged the OLR by approximately 1–5 days during the passage of Fani.

At N4, during the latter part of the summer monsoon, September–October 2018, a high coherence and 90° lag between HC_{26} (SST) and OLR were found roughly at a 20-day period (Figs. 18c,d); that is both SST and HC_{26} lagged the OLR by approximately 5 days. During this period, the upper 50-m layer was weakly stratified and close to the depth of the 26°C isotherm (Fig. 3f), U and V fluctuations were about $\pm$(20–30) cm s^{-1} (Fig. 2), and SSHA was negligible (Fig. 18a). Furthermore, wavelet spectral plots indicate that

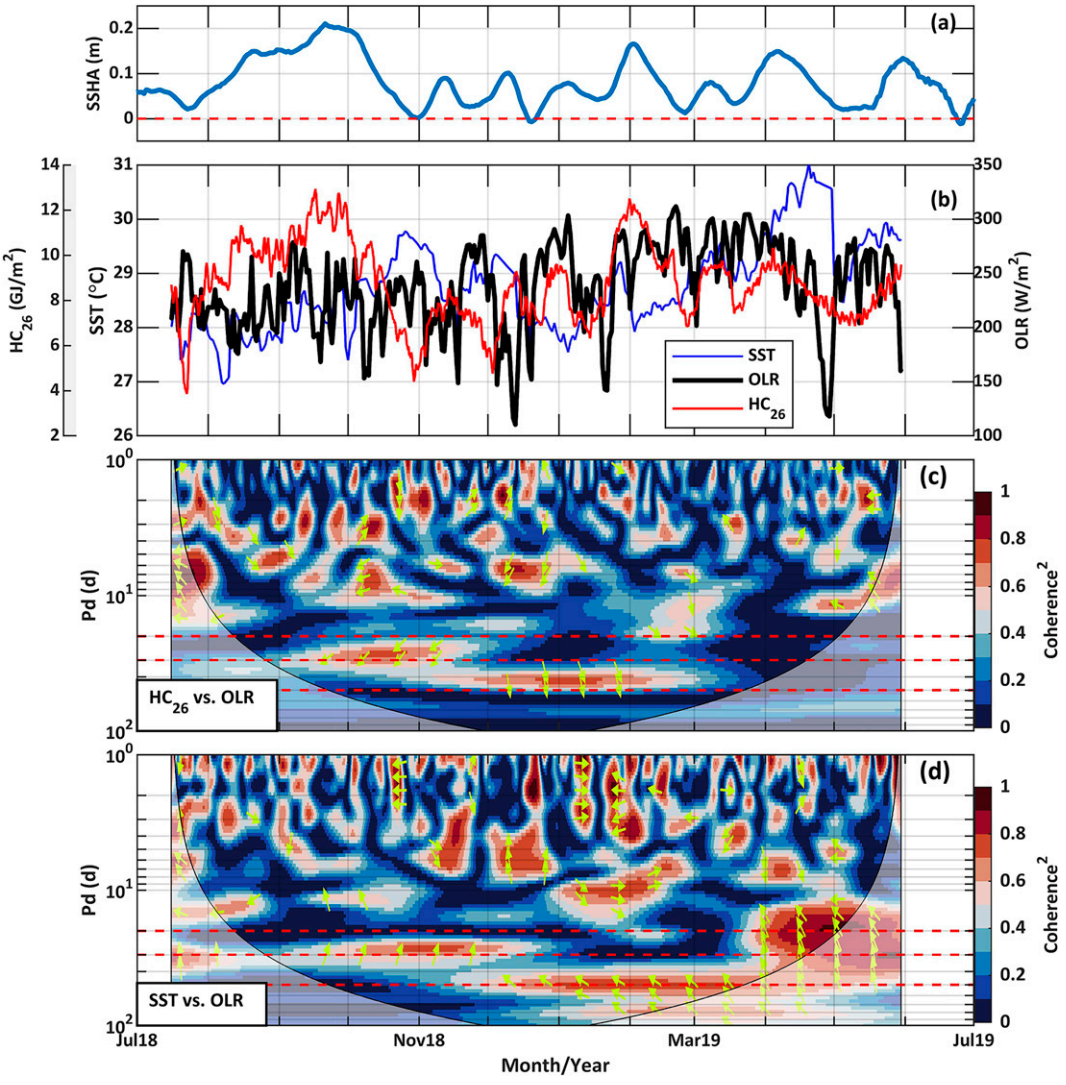

FIG. 19. As in Fig. 18, but for N1.

the event was associated with a negligible SSH anomaly (Fig. 11c), a clearly defined 26°C isotherm displacement (Fig. 11d) and moderate velocity variances (Figs. 11e,f). These observations indicate that both SST and HC_{26} anomalies were most likely generated by atmospheric forcing (e.g., MISO event), since SSH anomalies did not show clearly defined eddy/wave features (Fig. 18a). The observed lag between HC_{26}/SST and OLR is consistent with the previous findings (e.g., Sengupta et al. 2001; Krishnamurti et al. 2017). However, the relationships between SST–OLR and HC_{26}–OLR are not always consistent when HC_{26} is heavily influenced by the thermocline variability. For example, at N3, during August–October 2018, a high coherence and 90° phase lag between SST and OLR were found at a 15–30-day period, but no correlation was found between HC_{26} and OLR. During this period a cyclonic eddy (or cold eddy indicating an uplifted 26°C isotherm, Fig. 3g) passed through N3, thus lowering heat content as indicated in Figs. 13b,d (green lines).

However, for some instances heat content leads OLR. For example, at N1 (Fig. 19), HC_{26} led OLR for the 25–30-day band during October–November, and 40–50-day band during December–February. These periods coincided with passage of ISOs with positive SSH anomalies or anticyclonic features (Fig. 19a). Wavelet spectra shows strong SSH anomalies (Fig. 10c), large 26°C isotherm displacements (Fig. 10d), and large velocity anomalies (Figs. 10e,f). Therefore, it is likely that heat content associated with these ISOs (i.e., warm eddy like features, Fig. 19a) actively interacted with the atmospheric convection during fall and winter months. Similar large coherences were found between SST and OLR over these ISO events, but the SST lagged the OLR (Fig. 19d). We suspect that the surface heat flux associated with transient storms can alter SST rapidly, but that the surface forcing can be less effective in changing the thermal structure within the ISOs, which in turn can lead to the observed phase differences of SST and HC_{26} with OLR.

8. Summary and conclusions

Intraseasonal variability of currents, temperature, heat content, and heat fluxes, and correlations between ocean heat content and OLR as an indicator for atmospheric convection were examined from observations collected by moorings deployed in the central BoB, and by satellite. The major observational findings of this study are summarized below.

During the summer of 2018, the SMC in the upper 100 m was toward the northeast at about 30 cm s^{-1}, while hourly velocities in September were as large as 125 cm s^{-1}. The SMC passed between the cyclonic eddy (SLD) near N5 and the anticyclonic eddy near N1, and then turned toward the east while progressing between N1 and N2 (Fig. 7a). The volume transport of the SMC in the upper 200 m during July–September 2018 was about 4–5 Sv, and the transport in the layer between 200 and 600 m was less than 1 Sv. During winter, ISOs dominated in the upper 600 m (Fig. 7b).

The AVISO SSHAs show subseasonal (<120 day) variability during the 2018–19 period, The 10–60-day ISO band was found throughout the BoB, while the 60–90-day ISO band was limited to the southern BoB. Both ISOs propagated westward with speeds ranging from 10 to 30 cm s^{-1} with slower speeds toward the north, which is consistent with the previous estimates based on observations of currents and SSHA in the southcentral BoB (e.g., Pirro et al. 2020a,b).

Intraseasonal currents and thermocline temperature fluctuations with periods ranging from 10 to 60 days were observed throughout the year. The wavelet analysis revealed that 10-, 20-, 30-, and 40-day ISOs, found during summer and winter months did not follow a clear pattern at different mooring sites. Temperature ISOs with fluctuations as large as ±3°C were found in the thermocline between 50 and 100 m and velocity ISOs of 20–30 cm s^{-1} were found in the upper 200 m, and occasionally velocity fluctuations of 10–20 cm s^{-1} extended down to 600 m.

The heat content estimated over fixed depths (say 200 m) and above the 26°C isotherm shows strong ISO variability for periods from 10 to 60 days, similar to temperature ISOs, indicating thermocline temperature fluctuations dominate the heat content.

Wind stress and wind stress curl consisted of synoptic scales to 30 days, and seasonal variability. However, the occurrences of 30-day wind stress curl did not directly connect to the occurrences of 30-day oceanic ISOs as found along the mooring array. These two ISOs were separated by more than 3 months, suggesting that the westward-moving oceanic ISOs are most likely caused by remote forcing. However, local wind forcing is an important factor at N5, where the SLD forms, in which the thermocline domed during July–August, and is likely driven by local wind stress curl with Ekman pumping velocities as large as 1 m day^{-1}.

The wavelet cospectra-based heat-flux estimates show multiple ISOs (with periods of 10, 20, 30, 40, and 50 days) carry heat southward, and fluxes were strongest near 75 m depth, and decreased rapidly with depth. The time-averaged heat-flux profiles of 10–60-day ISOs, show largest fluxes between 50 and 100 m, and fluxes decreasing rapidly with depth. The meridional fluxes were larger than the zonal components except at N5, where the seasonally varying SLD influenced the eddy-flux estimates. The meridional heat fluxes averaged over a layer between 40 and 100 m had similar magnitudes at 8°, 10°, and 12°N, and were negligible at 14°N, indicating that strongest $\partial\overline{\langle V'T'\rangle}/\partial y$ occurred between 12° and 14°N. The 40–100-m layer-averaged $\partial\overline{\langle V'T'\rangle}/\partial y$ over the observational period was as large as 10^{-7} °C s^{-1}.

The estimated meridional heat-flux divergence, vertically integrated over the upper 200 m (i.e., $\int_0^H \rho C_p \partial\overline{\langle V'T'\rangle}/\partial y\, dz$ for H = 200 m) is 20–30 W m^{-2}, which is comparable to the annual average of net surface heat flux (~37 W m^{-2}) in the north-central bay. It is plausible that on an annual time scale, ISOs can transport surface heat flux southward, thus playing an important role in the upper-ocean heat balance.

The positive $\partial\overline{\langle V'T'\rangle}/\partial y$ tends to cool the layer. The estimated cooling equivalent to a rate of -10^{-7} °C s^{-1} for a period of one year is about 2°–3°C. The amount of cooling is a similar order of magnitude for the temperature drop in the upper 100 m (Figs. 8a–c and 4d) from spring to late summer/winter months, indicating that the meridional flux divergence can play a significant role in heat balance in the upper 100 m. In the lower part of thermocline between 100 and 200 m, $\partial\overline{\langle V'T'\rangle}/\partial y$ is about 2×10^{-8} °C s^{-1}, which can cool the thermocline about 0.5°C on annual time scales.

Coherence and phase between oceanic ISOs (HC_{26} and SST) and OLR at a 10–60-day band were examined using wavelet spectral methods. Phases and coherences between heat content and OLR, suggest that the OLR (an indirect measure of atmospheric convection) drives the upper-ocean thermal response during the summer monsoon period. The observed 4–5-day lag correlations between HC_{26}/SST and OLR are consistent with the previous findings (e.g., Sengupta et al. 2001; Krishnamurti et al. 2017). However, for some instances heat content leads OLR. The heat content associated with ISOs actively interacted with the atmospheric convection during fall and winter months. Similar large coherences were found between SST and OLR over these ISO events, but the SST lagged the OLR. It is likely that the surface buoyancy flux and wind stress forcing associated with transient storms can alter SST rapidly, but that the surface forcing could be less effective to change the thermal structure within ISOs, which in turn could lead to the observed phase differences of SST and HC_{26} with OLR.

This study suggests that oceanic ISOs (eddies/planetary waves) not only aid in transport of heat southward but also can play an active role in air–sea coupling at ISO time scales.

Acknowledgments. This work was sponsored by the U.S. Naval Research Laboratory project, Role of Indian Ocean on Monsoon Intraseasonal Oscillation (RIOMISO), and the U.S. Office of Naval Research (ONR) in an ONR Departmental Research Initiative (DRI), Monsoon Intraseasonal Oscillations in the Bay of Bengal (MISOBOB). Discussions with Drs.

Debasis Sengupta, Arnold Gordon, and Amit Tandon are greatly appreciated. The authors thank the two reviewers and the editor for their constructive comments. The NRL investigators were funded by ONR Grants N0001420WX00410 and N0001420WX01886. W. J. Teague and Z. R. Hallock were funded by ONR Grant N0001420WX01886. H.J.S. Fernando and investigators from Sri Lanka were funded by the ONR Grant N00014-17-1-2334. Special thanks to Mr. Andrew Quaid and Ian Martens for their efforts in preparation, deployment, and recovery of the moorings. The authors thank the captains and crews of the R/V *Thomas G. Thompson* and R/V *Sally Ride*.

Data availability statement. Community supported satellite data are available from https://www.aviso.altimetry.fr/en/data/products/sea-surface-height-products/global.html (sea surface height and associated geostrophic velocities); https://psl.noaa.gov/ (daily maps of SST); https://www.nrl.navy.mil/WindSat/ (daily maps of OLR, CLW, and rainfall); https://cds.climate.copernicus.eu/ (ECMWF-ERA5 reanalysis products); https://www.nrlmry.navy.mil/sat_products.html. RAMA mooring data sets are available at https://www.pmel.noaa.gov/tao/drupal/disdel/, and project-supported data sets are subjected to the signed agreement (memorandum of understanding) between the United States and Sri Lanka, and restrictions will apply until 2025. This time frame is intended to allow for students, postdoctoral fellows, and investigators supported under the project to have sufficient time to publish their results. After the restriction period, data may be requested from the corresponding author.

REFERENCES

Babu, M. T., Y. V. B. Sarma, V. S. N. Murthy, and P. Vethamony, 2003: On the circulation in the Bay of Bengal during northern spring inter-monsoon (March–April 1987). *Deep-Sea Res. II*, **5**, 855–865, https://doi.org/10.1016/S0967-0645(02)00609-4.

Chatterjee, A., D. Shankar, J. P. McCreary, P. N. Vinayachandran, and A. Mukherjee, 2017: Dynamics of Andaman Sea circulation and its role in connecting the equatorial Indian Ocean to the Bay of Bengal. *J. Geophys. Res. Oceans*, **122**, 3200–3218, https://doi.org/10.1002/2016JC012300.

Chen, G., Y. Li, Q. Xie, and D. Wang, 2018: Origins of eddy kinetic energy in the Bay of Bengal. *J. Geophys. Res. Oceans*, **123**, 2097–2115, https://doi.org/10.1002/2017JC013455.

Cheng, X., S.-P. Xie, J. P. McCreary, Y. Qi, and Y. Du, 2013: Intraseasonal variability of sea surface height in the Bay of Bengal. *J. Geophys. Res. Oceans*, **118**, 816–830, https://doi.org/10.1002/jgrc.20075.

——, J. P. McCreary, B. Qiu, Y. Qi, Y. Du, and X. Chen, 2018: Dynamics of eddy generation in the central Bay of Bengal. *J. Geophys. Res. Oceans*, **123**, 6861–6875, https://doi.org/10.1029/2018JC014100.

Cullen, K. E., and E. L. Shroyer, 2019: Seasonality and interannual variability of the Sri Lanka dome. *Deep Sea Res. II*, **168**, 104642, https://doi.org/10.1016/j.dsr2.2019.104642.

Dandapat, S., and A. Chakraborty, 2016: Mesoscale eddies in the Western Bay of Bengal as observed from satellite altimetry in 1993–2014: Statistical characteristics, variability and three-dimensional properties. *IEEE J. Sel. Top. Appl. Earth Obs. Remote Sens.*, **9**, 5044–5054, https://doi.org/10.1109/JSTARS.2016.2585179.

Flatau, M. K., P. J. Flatau, J. Schmidt, and G. N. Kiladis, 2003: Delayed onset of the 2002 Indian monsoon. *Geophys. Res. Lett.*, **30**, 1768, https://doi.org/10.1029/2003GL017434.

Fu, X., and B. Wang, 2004: Differences of boreal summer intraseasonal oscillations simulated in an atmosphere–ocean coupled model and an atmosphere-only model. *J. Climate*, **17**, 1263–1271, https://doi.org/10.1175/1520-0442(2004)017<1263:DOBSIO>2.0.CO;2.

——, ——, T. Li, and J. P. McCreary, 2003: Coupling between northward-propagating, intraseasonal oscillations and sea surface temperature in the Indian Ocean. *J. Atmos. Sci.*, **60**, 1733–1753, https://doi.org/10.1175/1520-0469(2003)060<1733:CBNIOA>2.0.CO;2.

——, ——, D. E. Waliser, and L. Tao, 2007: Impact of atmosphere–ocean coupling on the predictability of monsoon intraseasonal oscillations. *J. Atmos. Sci.*, **64**, 157–174, https://doi.org/10.1175/JAS3830.1.

Gadgil, S., 2003: The Indian monsoon and its variability. *Annu. Rev. Earth Planet. Sci.*, **31**, 429–467, https://doi.org/10.1146/annurev.earth.31.100901.141251.

——, P. A. Francis, and P. N. Vinayachandran, 2019: Summer monsoon of 2019: Understanding the performance so far and speculating about the rest of the season. *Curr. Sci.*, **117**, 783–793, https://doi.org/10.18520/cs/v117/i5/783-793.

Gao, Y., N. P. Klingaman, C. A. DeMott, and P.-C. Hsu, 2019: Diagnosing ocean feedbacks to the BSISO: SST-modulated surface fluxes and the moist static energy budget. *J. Geophys. Res. Atmos.*, **124**, 146–170, https://doi.org/10.1029/2018JD029303.

Girishkumar, M. S., M. Ravichandran, M. J. McPhaden, and R. R. Rao, 2011: Intraseasonal variability in barrier layer thickness in the south central Bay of Bengal. *J. Geophys. Res.*, **116**, C03009, https://doi.org/10.1029/2010JC006657.

——, ——, and W. Han, 2013: Observed intraseasonal thermocline variability in the Bay of Bengal. *J. Geophys. Res. Oceans*, **118**, 3336–3349, https://doi.org/10.1002/jgrc.20245.

Gordon, A. L., E. Shroyer, and V. S. N. Murty, 2017: An intrathermocline eddy and a tropical cyclone in the Bay of Bengal. *Sci. Rep.*, **7**, 46218, https://doi.org/10.1038/srep46218.

Goswami, B. N., 2005: South Asian monsoon. *Intraseasonal Variability in the Atmosphere-Ocean Climate System*, W. K. Lau and D. E. Waliser, Eds., Springer, 19–61, https://doi.org/10.1007/3-540-27250-X_2.

——, D. Sengupta, and G. S. Kumar, 1998: Intraseasonal oscillations and interannual variability of surface winds over the Indian monsoon region. *Proc. Indian Acad. Sci., Earth Planet. Sci.*, **107**, 45–64, https://doi.org/10.1007/BF02842260.

——, R. S. Ajayamohan, P. K. Xavier, and D. Sengupta, 2003: Clustering of synoptic activity by Indian summer monsoon intraseasonal oscillations. *Geophys. Res. Lett.*, **30**, 1431, https://doi.org/10.1029/2002GL016734.

Grinsted, A., 2021: Cross wavelet and wavelet coherence. GitHub, https://github.com/grinsted/wavelet-coherence.

——, J. C. Moore, and S. Jevrejeva, 2004: Application of the cross wavelet transform and wavelet coherence to geophysical time series. *Nonlinear Processes Geophys.*, **11**, 561–566, https://doi.org/10.5194/npg-11-561-2004.

Grossmann, A., and J. Morlet, 1984: Decomposition of Hardy functions into square integrable wavelet of constant shape. *SIAM J. Math. Anal.*, **15**, 723–736, https://doi.org/10.1137/0515056.

Hacker, P., E. Firing, J. Hummon, A. L. Gordon, and J. C. Kindle, 1998: Bay of Bengal currents during the northeast monsoon. *Geophys. Res. Lett.*, **25**, 2769–2772, https://doi.org/10.1029/98GL52115.

Han, W., 2005: Origins and dynamics of the 90-day and 30–60-day variations in the equatorial Indian Ocean. *J. Phys. Oceanogr.*, **35**, 708–728, https://doi.org/10.1175/JPO2725.1.

——, J. P. McCreary Jr., D. L. T. Anderson, and A. J. Mariano, 1999: Dynamics of the eastern surface jets in the equatorial Indian Ocean. *J. Phys. Oceanogr.*, **29**, 2191–2209, https://doi.org/10.1175/1520-0485(1999)029<2191:DOTESJ>2.0.CO;2.

Han, W. Q., D. M. Lawrence, and P. J. Webster, 2001: Dynamical response of equatorial Indian Ocean to intraseasonal winds: Zonal flow. *Geophys. Res. Lett.*, **28**, 4215–4218, https://doi.org/10.1029/2001GL013701.

Hwang, P. A., 2011: A note on the ocean surface roughness spectrum. *J. Atmos. Oceanic Technol.*, **28**, 436–443, https://doi.org/10.1175/2010JTECHO812.1.

Jaimes, B., L. K. Shay, and J. K. Brewster, 2016: Observed air-sea interactions in tropical cyclone Isaac over loop current mesoscale eddy features. *Dyn. Atmos. Oceans*, **76**, 306–324, https://doi.org/10.1016/j.dynatmoce.2016.03.001.

Kemball-Cook, S., and B. Wang, 2001: Equatorial waves and air-sea interaction in the boreal summer intraseasonal oscillation. *J. Climate*, **16**, 2923–2942, https://doi.org/10.1175/1520-0442(2001)014<2923:EWAASI>2.0.CO;2.

Kripalani, R. H., A. Kulkarni, S. S. Sabade, J. V. Revadekar, S. K. Patwardhan, and J. R. Kulkarni, 2004: Intra-seasonal oscillations during monsoon 2002 and 2003. *Curr. Sci.*, **87**, 325–331.

Krishnamurti, T., and P. Ardanuy, 1980: The 10 to 20-day westward propagating mode and "breaks in the monsoons." *Tellus*, **32**, 15–26, https://doi.org/10.3402/tellusa.v32i1.10476.

——, S. Jana, R. Krishnamurti, V. Kumar, R. Deepa, F. Papa, M. A. Bourassa, and M. M. Ali, 2017: Monsoonal intraseasonal oscillations in the ocean heat content over the surface layers of the Bay of Bengal. *J. Mar. Syst.*, **167**, 19–32, https://doi.org/10.1016/j.jmarsys.2016.11.002.

Kurien, P., M. Ikeda, and V. K. Valsala, 2010: Mesoscale variability along the east coast of India in spring as revealed from satellite data and OGCM simulations. *J. Oceanogr.*, **66**, 273–289, https://doi.org/10.1007/s10872-010-0024-x.

Laxague, N. J., B. K. Haus, D. G. Ortiz-Suslow, and H. C. Graber, 2018: Quantifying highly variable air–sea momentum flux using wavelet analysis. *J. Atmos. Oceanic Technol.*, **35**, 1849–1863, https://doi.org/10.1175/JTECH-D-18-0064.1.

Leipper, D., and D. Volgenau, 1972: Hurricane heat potential of the Gulf of Mexico. *J. Phys. Oceanogr.*, **2**, 218–224, https://doi.org/10.1175/1520-0485(1972)002<0218:HHPOTG>2.0.CO;2.

Lueck, R., F. Wolk, J. Hancyck, and K. Black, 2015: Hub-height time series measurements of velocity and dissipation of turbulence kinetic energy in a tidal channel. *IEEE/OES 11th Current, Waves and Turbulence Measurement (CWTM)*, St. Petersburg, FL, Institute of Electrical and Electronics Engineers, 1–5, https://doi.org/10.1109/CWTM.2015.7098143.

Luecke, C. A., H. W. Wijesekera, E. Jarosz, D. W. Wang, J. C. Wesson, S. U. P. Jinadasa, H. J. S. Fernando, and W. J. Teague, 2021: Observations of eddy-modulated turbulent mixing in the southern Bay of Bengal. *J. Phys. Oceanogr.*, **51**, 2149–2166, https://doi.org/10.1175/JPO-D-20-0280.1.

Mallat, S. G., 1989: A theory for multiresolution signal decomposition: The wavelet representation. *IEEE Trans. Pattern Anal. Mach. Intell.*, **11**, 674693, https://doi.org/10.1109/34.192463.

McPhaden, M. J., and Coauthors, 2009: RAMA: The Research Moored Array for African–Asian–Australian Monsoon Analysis and Prediction. *Bull. Amer. Meteor. Soc.*, **90**, 459–480, https://doi.org/10.1175/2008BAMS2608.1.

Miyama, T., J. P. McCreary Jr., T. G. Jensen, D. Sengupta, and R. Senan, 2006: Dynamics of biweekly oscillations in the equatorial Indian Ocean. *J. Phys. Oceanogr.*, **36**, 827–846, https://doi.org/10.1175/JPO2897.1.

Mohanty, S., R. Nadimpalli, U. C. Mohanty, M. Mrutyunjay, A. Sherma, A. K. Das, and S. Sil, 2020: Quasi-operational forecast guidance of extremely severe cyclonic storm Fani over the Bay of Bengal using high-resolution mesoscale models. *Meteor. Atmos. Phys.*, **133**, 331–348, https://doi.org/10.1007/s00703-020-00751-4.

Moore, D. W., 1968: Planetary-gravity waves in an equatorial ocean. Ph.D. thesis, Harvard University, 207 pp.

Morlet, J., G. Arens, E. Fourgeau, and D. Giard, 1982: Wave propagation and sampling theory—Part I: Complex signal and scattering in multilayered media. *Geophysics*, **47**, 203–221, https://doi.org/10.1190/1.1441328.

Nagura, M., and M. J. McPhaden, 2010: Dynamics of zonal current variations associated with the Indian Ocean dipole. *J. Geophys. Res.*, **115**, C11026, https://doi.org/10.1029/2010JC006423.

Pirro, A., H. W. Wijesekera, E. Jarosz, and H. J. S. Fernando, 2020a: Dynamics of intraseasonal oscillations in the Bay of Bengal during summer monsoons captured by mooring observations. *Deep-Sea Res. II*, **172**, 104718, https://doi.org/10.1016/j.dsr2.2019.104718.

——, H. J. S. Fernando, H. W. Wijesekera, T. G. Jensen, L. R. Centurioni, and S. U. P. Jinadasa, 2020b: Eddies and currents in the Bay of Bengal during summer monsoons. *Deep-Sea Res. II*, **172**, 104728, https://doi.org/10.1016/j.dsr2.2019.104728.

Prasanna Kumar, S., and Coauthors, 2004: Are eddies nature's trigger to enhance biological productivity in the Bay of Bengal? *Geophys. Res. Lett.*, **31**, L07309, https://doi.org/10.1029/2003GL019274.

Ratna, S. B., A. Cherchi, T. J. Osborn, M. Joshi, and U. Uppara, 2021: The extreme positive Indian Ocean dipole of 2019 and associated Indian summer monsoon rainfall response, *Geophys. Res. Lett.*, **48**, e2020GL091497, https://doi.org/10.1029/2020GL091497.

Sanchez-Franks, A., E. C. Kent, A. J. Matthews, B. G. M. Webber, S. C. Peatman, and P. N. Vinayachandran, 2018: Intraseasonal variability of air-sea fluxes over the Bay of Bengal during the southwest monsoon. *J. Climate*, **31**, 7087–7109, https://doi.org/10.1175/JCLI-D-17-0652.1.

Sengupta, D., and M. Ravichandran, 2001: Oscillations of Bay of Bengal sea surface temperature during the 1998 summer monsoon. *Geophys. Res. Lett.*, **28**, 2033–2036, https://doi.org/10.1029/2000GL012548.

——, B. N. Goswami, and R. Senan, 2001: Coherent intraseasonal oscillations of ocean and atmosphere during the Asian summer monsoon. *Geophys. Res. Lett.*, **28**, 4127–4130, https://doi.org/10.1029/2001GL013587.

——, R. Senan, V. S. N. Murty, and V. Fernando, 2004: A biweekly mode in the equatorial Indian Ocean. *J. Geophys. Res.*, **109**, C10003, https://doi.org/10.1029/2004JC002329.

Sharmila, S., and Coauthors, 2013: Role of ocean–atmosphere interaction on northward propagation of Indian summer monsoon intra-seasonal oscillations (MISO). *Climate Dyn.*, **41**, 1651–1669, https://doi.org/10.1007/s00382-013-1854-1.

Shroyer, E., and Coauthors, 2021: Bay of Bengal intraseasonal oscillations and the 2018 monsoon onset. *Bull. Amer. Meteor. Soc.*, **102**, E1936–E1951, https://doi.org/10.1175/BAMS-D-20-0113.1.

Tennekes, H., and J. L. Lumley, 1972: *A First Course in Turbulence*. The MIT Press, 300 pp.

Torrence, C., and G. P. Compo, 1998: A practical guide to wavelet analysis. *Bull. Amer. Meteor. Soc.*, **79**, 61–78, https://doi.org/10.1175/1520-0477(1998)079<0061:APGTWA>2.0.CO;2.

Vidya, P. J., and S. Prasanna Kumar, 2013: Role of mesoscale eddies on the variability of biogenic flux in the northern and central Bay of Bengal. *J. Geophys. Res. Oceans*, **118**, 5760–5771, https://doi.org/10.1002/jgrc.20423.

Webber, B. G. M., A. J. Matthews, P. N. Vinayachandran, C. P. Neema, A. Sanchez-Franks, V. Vijith, P. Amol, and D. B. Baranowski, 2018: The dynamics of the southwest monsoon current in 2016 from high-resolution in situ observations and models. *J. Phys. Oceanogr.*, **48**, 2259–2282, https://doi.org/10.1175/JPO-D-17-0215.1.

Weller, R. A., J. T. Farrar, H. Seo, C. Prend, D. Sengupta, J. S. Lekha, M. Ravichandran, and R. Venkatesen, 2019: Moored observations of the surface meteorology and air–sea fluxes in the northern Bay of Bengal in 2015. *J. Climate*, **32**, 549–573, https://doi.org/10.1175/JCLI-D-18-0413.1.

Wijesekera, H. W., W. J. Teague, D. W. Wang, E. Jarosz, and T. G. Jenson, 2016: Low frequency currents from deep moorings in the Southern Bay of Bengal. *J. Phys. Oceanogr.*, **46**, 3209–3237, https://doi.org/10.1175/JPO-D-16-0113.1.

Willebrand, J., S. G. H. Philander, and R. C. Pacanowski, 1980: The oceanic response to large-scale atmospheric disturbances. *J. Phys. Oceanogr.*, **10**, 411–429, https://doi.org/10.1175/1520-0485(1980)010<0411:TORTLS>2.0.CO;2.

Wunsch, C., 1997: The vertical partition of oceanic horizontal kinetic energy. *J. Phys. Oceanogr.*, **27**, 1770–1794, https://doi.org/10.1175/1520-0485(1997)027<1770:TVPOOH>2.0.CO;2.

Wyrtki, K., 1973: An equatorial jet in the Indian Ocean. *Science*, **181**, 262–264, https://doi.org/10.1126/science.181.4096.262.

Yu, L., X. Jin, and R. A. Weller, 2007: Annual, seasonal, and interannual variability of air–sea heat fluxes in the Indian Ocean. *J. Climate*, **20**, 3190–3209, https://doi.org/10.1175/JCLI4163.1.

Zhou, L., and R. Murtugudde, 2014: Impact of northward-propagating intraseasonal variability on the onset of Indian summer monsoon. *J. Climate*, **27**, 126–139, https://doi.org/10.1175/JCLI-D-13-00214.1.